bioRxiv preprint doi: https://doi.org/10.1101/2021.05.02.442342; this version posted May 2, 2021. The copyright holder for this preprint (which was not certified by peer review) is the author/funder, who has granted bioRxiv a license to display the preprint in perpetuity. It is made available under aCC-BY-NC-ND 4.0 International license.

Cytosolic aggregation of mitochondrial proteins disrupts cellular homeostasis by stimulating other proteins aggregation.

Urszula Nowicka[1,2], Piotr Chroscicki[1,3,6], Karen Stroobants[4,6], Maria Sladowska[1,3], Michal Turek[1,3,5], Barbara Uszczynska-Ratajczak[1,3], Rishika Kundra[4], Tomasz Goral[1,5], Michele Perni[4], Christopher M. Dobson[4], Michele Vendruscolo[4] & Agnieszka Chacinska[1,2,5,*]

[1]*Centre of New Technologies, University of Warsaw, 02-097 Warsaw, Poland*

[2]*IMol Polish Academy of Sciences, 00-783 Warsaw, Poland*

[3]*International Institute of Molecular and Cell Biology, 02-109 Warsaw, Poland*

[4]*Centre for Misfolding Diseases, Department of Chemistry, University of Cambridge, Cambridge CB2 1EW, United Kingdom*

[5]*ReMedy International Research Agenda Unit, University of Warsaw, Warsaw 02-097, Poland*

[6]These authors contributed equally to this work

*Correspondence should be directed to a.chacinska@cent.uw.edu.pl

bioRxiv preprint doi: https://doi.org/10.1101/2021.05.02.442342; this version posted May 2, 2021. The copyright holder for this preprint (which was not certified by peer review) is the author/funder, who has granted bioRxiv a license to display the preprint in perpetuity. It is made available under aCC-BY-NC-ND 4.0 International license.

Abstract

Mitochondria are organelles with their own genomes but rely on the import of nuclear-encoded proteins synthesized by cytosolic ribosomes. Therefore, it is important to understand whether failures in the mitochondrial uptake of these nuclear-encoded proteins may cause proteotoxic stress, and to identify which response mechanisms may be in place to respond to it. Here, we report that upon mitochondrial protein import impairment, high-risk precursor and immature forms of mitochondrial proteins form aberrant deposits in the cytosol. In turn, these deposits cause further cytosolic accumulation of other mitochondrial and disease-related proteins, including α-synuclein and amyloid β. This aberrant accumulation triggers a cytosolic protein homeostasis imbalance that is accompanied by specific molecular chaperone responses, both at the transcriptomic and protein levels. Our results provide evidence that mitochondrial dysfunction, and specifically protein import defects, can contribute to protein homeostasis impairment, thus revealing a possible molecular mechanism for mitochondrial involvement in neurodegenerative diseases.

Introduction

Although more than a thousand proteins are required for mitochondria to perform their functions, only about 1% of them are synthesized inside this organelle. Therefore, the majority of mitochondrial proteins synthesized in the cytosol must be actively transported to mitochondria, a process that takes place via a sophisticated system of protein translocases and sorting machineries (Calvo, Clauser, & Mootha, 2016; Morgenstern et al., 2017; Neupert & Herrmann, 2007; Pfanner, Warscheid, & Wiedemann, 2019). The consequences of mitochondrial protein import defects on the cellular proteostasis are severe, but we currently know only a few response mechanisms that are able to respond to it (Boos et al., 2019; Izawa, Park, Zhao, Hartl, & Neupert, 2017; Kim et al., 2016; Martensson et al., 2019; Priesnitz &

bioRxiv preprint doi: https://doi.org/10.1101/2021.05.02.442342; this version posted May 2, 2021. The copyright holder for this preprint (which was not certified by peer review) is the author/funder, who has granted bioRxiv a license to display the preprint in perpetuity. It is made available under aCC-BY-NC-ND 4.0 International license.

Becker, 2018; Wang & Chen, 2015; Weidberg & Amon, 2018; Wrobel et al., 2015; Wu et al., 2019). Mitochondrial dysfunction is indeed a hallmark of neurodegenerative disorders, as mitochondrial defects such as Ca^{2+} handling, reactive oxygen species (ROS) increase, electron transport chain (ETC) inhibition, impairment in ER-mitochondria tethering are well described pathological markers (Cabral-Costa & Kowaltowski, 2020). It is still not known, however, if mitochondrial defects are consequences of neurodegeneration, or if they can contribute to it, or both. On one side, disease-related proteins can interfere with mitochondrial import and further processing of imported proteins within mitochondria (Cenini, Rub, Bruderek, & Voos, 2016; Di Maio et al., 2016; Mossmann et al., 2014; Vicario, Cieri, Brini, & Cali, 2018). Furthermore, aggregated proteins can be imported into mitochondria where they can be either cleared or sequestered in specific deposit sites (Bruderek et al., 2018; Ruan et al., 2017; Sorrentino et al., 2017). However, the reverse aspect of how mitochondrial dysfunctions, including mitochondrial import defects, contribute to the progression of neurodegenerative diseases remains elusive. A possible mechanism can be through altered cellular homeostasis, as mitochondrial dysfunctions affect it in many ways (Andreasson, Ott, & Buttner, 2019; Braun & Westermann, 2017; Escobar-Henriques, Altin, & Brave, 2020).

Recently, it has been shown that mitochondrial proteins import impairment, as well as overloading of mitochondrial import machineries, results in the accumulation of mitochondria-targeted proteins in the cytosol and stimulation of mitoprotein-induced stress (Boos et al., 2019; Wang & Chen, 2015; Wrobel et al., 2015). The question arises of, whether the accumulation of mistargeted mitochondrial proteins contributes to the progression of neurodegeneration at the cellular level. Additionally, one would like to understand whether mitoprotein-induced stress is a general response to all precursor proteins that globally accumulate in the cytosol, and if there is a subset of mitochondrial precursor proteins that pose difficult challenges to the protein

bioRxiv preprint doi: https://doi.org/10.1101/2021.05.02.442342; this version posted May 2, 2021. The copyright holder for this preprint (which was not certified by peer review) is the author/funder, who has granted bioRxiv a license to display the preprint in perpetuity. It is made available under aCC-BY-NC-ND 4.0 International license.

homeostasis system, and consequently may contribute to the onset and progression of neurodegenerative disorders (Boos, Labbadia, & Herrmann, 2020).

The analysis of a transcriptional signature of Alzheimer's disease supports the notion that there is a subset of mitochondrial proteins that are more dangerous than others for the cell (Ciryam et al., 2016; Kundra, Ciryam, Morimoto, Dobson, & Vendruscolo, 2017). These studies have shown that specific mitochondrial proteins functionally related to oxidative phosphorylation are transcriptionally down-regulated in Alzheimer's disease. Here we addressed the question of why these proteins are downregulated. As a poin of attack, we hypothesized that this need arises from the potential metastable properties of these proteins. Indeed, we found that when some of these mitochondrial proteins remained in the cytosol, due to mitochondrial protein import insufficiency, they formed insoluble aggregates disrupting protein homeostasis in the cell. These proteins triggered a prompt specific molecular chaperone response aimed at minimizing the consequences of protein aggregation. However, if this rescue mechanism was not sufficient, these aggregates stimulated the cytosolic aggregation of other mitochondrial proteins, and led to the downstream aggregation of non-mitochondrial proteins. Thus, our results indicate that metastable mitochondrial proteins could be transcriptionally downregulated during neurodegeneration in order to minimize cellular protein homeostasis imbalance caused by their mistargeting.

Results

Metastable mitochondrial precursor proteins can aggregate in the cytosol

The analysis of a transcriptomic signature of Alzheimer's disease identified oxidative phosphorylation as a pathway metastable and downregulated in the human central nervous system (Ciryam et al., 2016; Kundra et al., 2017). This observation suggests that a group of mitochondrial proteins might be dangerous for cellular protein homeostasis due to their poor

bioRxiv preprint doi: https://doi.org/10.1101/2021.05.02.442342; this version posted May 2, 2021. The copyright holder for this preprint (which was not certified by peer review) is the author/funder, who has granted bioRxiv a license to display the preprint in perpetuity. It is made available under aCC-BY-NC-ND 4.0 International license.

solubility at their cellular concentrations. We selected these mitochondrial genes from KEGG analysis and identified their yeast homologs when possible (**Figure 1–figure supplement 1**). Based on the yeast homologs sequence, we generated FLAG-tagged constructs expressed under the control of the copper-inducible promoter (CUP1). Next, we established a multi-centrifugation step assay to assess whether or not these proteins, when overproduced, exceed their critical concentrations and become supersaturated (Vecchi et al., 2020), thus acquiring the ability to aggregate during their trafficking to mitochondria (**Figure 1–figure supplement 2A**). We followed a FLAG peptide signal to evaluate if the protein was present in the soluble (S_{125k}) or insoluble (P_{125k}) fraction. We found that subunits β and g of the mitochondrial F_1F_O ATP synthase (Atp2 and Atp20, respectively) were present in the insoluble fraction, indicating that they formed high-molecular-weight deposits (**Figure 1A** and **Figure 1–figure supplement 2B**). We made a similar observation for the Rieske iron-sulfur ubiquinol-cytochrome *c* reductase (Rip1). Rip1 and subunit VIII of cytochrome *c* oxidase complex IV (Cox8) had their precursor forms entirely insoluble, whereas the mature forms were partially insoluble (the precursor form of the protein is bigger in size and migrates on the gel above the mature form) (**Figure 1A** and **Figure 1–figure supplement 2C**). Furthermore, the mature forms of subunit 8 of ubiquinol cytochrome *c* reductase, complex III (Qcr8), the core subunit of the ubiquinol-cytochrome *c* reductase complex (Cor1), and the subunit β of the mitochondrial processing protease, MPP (Mas1) were found partially insoluble. Only subunit VIb of cytochrome *c* oxidase (Cox12) and subunit 6 of ubiquinol cytochrome *c* reductase complex (Qcr6) were mainly present in the soluble fraction (**Figure 1A** and **Figure 1–figure supplement 2B**). Moreover, the tendency to aggregate and its harmful consequences correlated well with growth defects of yeast strains under oxidative conditions when galactose was used as a carbon source (**Figure 1B**). Higher the amount of an overproduced protein in the insoluble fraction, the bigger increase in lethality was observed. The difference was still present under the heat shock of

bioRxiv preprint doi: https://doi.org/10.1101/2021.05.02.442342; this version posted May 2, 2021. The copyright holder for this preprint (which was not certified by peer review) is the author/funder, who has granted bioRxiv a license to display the preprint in perpetuity. It is made available under aCC-BY-NC-ND 4.0 International license.

37 °C, indicating that general chaperone response associated with an increase of the temperate could not compensate for the observed changes for Atp2, Cox8, pRip1 and could only partially compensate in case of Cox12 and Atp20. Furthermore, the growth defect disappeared under the condition of fermentative respiration (**Figure 1–figure supplement 2D**). Interestingly, when glucose was used as a carbon source, a gain of stress resistance was observed upon the overproduction of Atp20, suggesting protective mechanism stimulation.

To test whether these metastable mitochondrial proteins aggregate in the cytosol as a result of an inefficient mitochondrial protein import system, we followed the cytosolic fate of non-imported mitochondrial proteins containing a cleavable targeting sequence. In agreement with the previous studies (Wrobel et al., 2015), cells treated with a chemical uncoupler, carbonyl cyanide m-chlorophenyl hydrazine (CCCP) have a compromised mitochondrial inner membrane electrochemical potential (IM potential) and protein import failure (Chacinska, Koehler, Milenkovic, Lithgow, & Pfanner, 2009; Neupert & Herrmann, 2007; van der Laan, Hutu, & Rehling, 2010). To ensure sufficient conditions to observe import defects, but not to extended negative consequences of using CCCP such as autophagy, the treatment time was limited to 30 min. The perturbed IM potential resulted in the accumulation of the precursor forms of Rip1 (pRip1), similarly as at the condition when Rip1 was overproduced (**Figure 1C** and **Figure 1–figure supplement 2E**). We also extended the analysis for the precursor form of the other proteins for which antibodies were available at the laboratory and allowed for precursor forms detection, namely: the mitochondrial matrix superoxide dismutase (Sod2), and mitochondrial malate dehydrogenase 1 (Mdh1) (**Figure 1C** and **Figure 1–figure supplement 2E**). The accumulation of pRip1, as well as the precursor form of Sod2 (pSod2), and precursor form of Mdh1 (pMdh1) were increasing with increasing CCCP concentration (**Figure 1D**). Next, the aggregation assay was performed to assess the fate of precursor mitochondrial proteins under chemical impairment of mitochondrial import. The pRip, pSod2, and pMdh1

bioRxiv preprint doi: https://doi.org/10.1101/2021.05.02.442342; this version posted May 2, 2021. The copyright holder for this preprint (which was not certified by peer review) is the author/funder, who has granted bioRxiv a license to display the preprint in perpetuity. It is made available under aCC-BY-NC-ND 4.0 International license.

forms were present in the pellet fractions, demonstrating that even without overproduction they also formed insoluble aggregates in the cell (**Figure 1E**). We also tested the conditions of defective protein import by using a temperature-sensitive mutant of TIM23 presequence translocase, *pam16-3*(Wrobel et al., 2015). The precursor forms of Rip1 and Sod2 accumulated (**Figure 1F**) and consequently formed insoluble aggregates at this conditions (**Figure 1–figure supplement 2F**). Therefore, the mistargeted precursor forms of mitochondrial proteins aggregate when their concentration exceeds their solubility point, as observed both when mitochondrial metastable proteins were overproduced, and when the defect of mitochondrial import was stimulated chemically, or by employing mutants of the presequence translocases import pathway.

Mitochondrial proteins aggregation stimulates a cytosolic molecular chaperone response

To further investigate a cellular response, we determined global transcriptomic changes triggered by the pRip1 overproduction and *pam16-3* mutation (**Figure2-Source Data 1-4**). Our time-series analysis revealed groups of differentially expressed genes (**Figure 2A** and **2B,** and **Figure2–figure supplement 1A**). pRip1 overexpression introduced small, rather specific changes to the transcriptome, wherein a total of 9 genes were up- and 4 were down-regulated, all listed in the Fig 2C. The KEGG analysis identified oxidative phosphorylation pathway to be upregulated as expected by the pRip1 overexpression (**Figure2–figure supplement 1B**). Interestingly, the second upregulated KEGG pathway was ABC transporters, but after extensive pRpi1 production for more than 4 hours (**Figure2–figure supplement 1B**). Moreover, in the case of pRip1, the biggest fold change was observed for the *SSA1*, *SSA4*, and *HSP82* chaperones being a probable response mechanism to pRip1 aggregation (**Figure 2A** and **2C)**. Nevertheless, the extended pRip1 overproduction, started to reflect on mitochondrial performance as mitochondria associated genes, *POT1*, *DLD3*, *AGP3*, *PDC6*, became down-regulated (**Figure**

bioRxiv preprint doi: https://doi.org/10.1101/2021.05.02.442342; this version posted May 2, 2021. The copyright holder for this preprint (which was not certified by peer review) is the author/funder, who has granted bioRxiv a license to display the preprint in perpetuity. It is made available under aCC-BY-NC-ND 4.0 International license.

2C). Furthermore, the effect of *pam16-3* mutation was stronger and, perhaps unsurprisingly (Wrobel et al., 2015), down-regulated the expression of genes related to the oxidative phosphorylation, metabolic, citrate cycle, and biosynthesis of secondary metabolites pathways (**Figure2–figure supplement 1C**). More than half of the genes affected were coding for mitochondrial proteins (Morgenstern et al., 2017) (**Figure2–figure supplement 1D**). Furthermore, we wanted to test if, similarly as for when pRip1 overexpression, the chaperone genes would also be upregulated in case of *pam16-3* mutation. Therefore, we analysed all genes that were significantly changed and selected those with chaperones function (**Figure 2D**). Indeed, the *pam16-3* mutation affected a series of genes encoding for molecular chaperones. We observed the upregulation of *HSP82* and *SSA4* genes, which were also upregulated in case of pRip1 overexpression. We also observed upregulation of others chaperone genes e.g.: *SNO4, HSP26, HSP42, SSE2, HSP12, HSP32, HSP104, HSP33* (**Figure 2B** (blue) and **2D).** Since we used a temperature-sensitive mutant *pam16-3*, we wanted to test if the observed chaperones' genes upregulation was specific to the mitochondrial dysfunction effects, and not due to the heat shock treatment. For that purpose, we compared the changes in the wild-type samples both at 19 $^{\circ}$C and 37 $^{\circ}$C and compared them to the corresponding changes in the *pam16-3* mutant **(Figure2–figure supplement 1E)**. Our analysis showed that the chaperone response in *pam16-3* went beyond the changes expected just for the high-temperature treatment. In particular, the most pronounced change was observed for *SSE2, SIS1, HSP42* and *HSP104* at 4 hours of treatment (**Figure2–figure supplement 1E,** black arrows). This suggested that impairment of mitochondrial import originating from defects of translocases had a similar consequence as clogging the import sites (Boos et al., 2019). Again, to compare pRip1 data with the effects of *pam16-3* mutation, we wanted to check if the ABC-transporter's genes would also be upregulated. The analysis of significantly changed genes showed that with extended of time the *PDR5* gene levels were changed, as well as other ABS-transporters: *PDR15, SNQ2* (**Figure2–**

bioRxiv preprint doi: https://doi.org/10.1101/2021.05.02.442342; this version posted May 2, 2021. The copyright holder for this preprint (which was not certified by peer review) is the author/funder, who has granted bioRxiv a license to display the preprint in perpetuity. It is made available under aCC-BY-NC-ND 4.0 International license.

figure supplement 1F). The *PDR5* is controlled by the PDR3 transcription factor (Gulshan, Schmidt, Shahi, & Moye-Rowley, 2008), which gene levels also increased. Interestingly all these genes were identified to be involved in the MitoCPR response (Weidberg & Amon, 2018). When we extended our analysis to other MitoCPR related genes, we observed their upregulation starting at 4 hours of treatment (**Figure2–figure supplement 1F**).

Next, we wanted to assess if the observed molecular chaperone upregulation would also be observed at the protein level. We used CCCP to stimulate the mitochondrial dysfunction to avoid the temperature factor at the initial screening. We monitored the changes of the protein levels for all chaperones against which we had antibodies available at the time of the studies: Hsp104, Ssa1, Ssb1, Ssc1, Hsp60, Edg1. While no changes were observed for most of the them, a significant response was observed for Hsp104 chaperone (**Figure 3A** and **3B)**. Remarkably, the Hsp104 upregulation on the protein level was observed already after 15 min of treatment (**Figure3–figure supplement 1A**). Furthermore, we tested if the Hsp104 protein was upregulated in response to mitochondrial import defects caused by *pam16-3* mutation, along with established *pam16-1* and *pam18-1* mutants, and MIA import pathway mutations, *mia40-4int* and *mia40-3(Wrobel et al., 2015)*. For all of the mutants at the permissive conditions (19 °C), when just a mild induction protein import phenotypes take place, we observed upregulation of Hsp104 chaperone at the protein level (**Figure 3C**). This effect was still present at the restrictive conditions 37 °C, but the differences were less eminent due to the activation of heat shock responses (**Figure3–figure supplement 1B**). We also wanted to test if the Hsp42 chaperone would be upregulated on the protein level since its upregulation was one of the most prominent based on the transcriptomic data for *pam16-3* mutant. Due to the lack of the antibody against Hsp42 chaperone, we used a yeast strain with *hsp42* tagged with GFP, that allowed for following Hsp42 protein levels by monitoring the GFP signal. We could only test the consequences of mitochondrial import impairment caused by CCCP treatment, in such an

bioRxiv preprint doi: https://doi.org/10.1101/2021.05.02.442342; this version posted May 2, 2021. The copyright holder for this preprint (which was not certified by peer review) is the author/funder, who has granted bioRxiv a license to display the preprint in perpetuity. It is made available under aCC-BY-NC-ND 4.0 International license.

experimental setup. With an agreement to the transcriptomic data of *pam16-3*, we observed the increased abundance of Hsp42 protein (**Figure 3D)**. Having identified Hsp42 and Hsp104 as two chaperones that change significantly when the mitochondrial import is impaired, we examined their expression levels when metastable mitochondrial proteins were overproduced. The Hsp104 protein levels were significantly upregulated upon such protein overproduction (**Figure 3E** and **3F**). The Hsp42 levels were again analysed in the background of *hsp42-GFP* strain, and here we also observed an increased abundance of Hsp42 chaperone for all of the metastable proteins (**Figure 3G** and **3H)**. Interestingly, in the case of pRip1, this response was not observed at the transcriptome levels, but it was significant at the protein levels (**Figure 2C vs. Figure 3G** and **3H)**. Thus, upregulation of a specific molecular chaperones in response to cytosolic mitochondrial protein aggregation can be performed both transcriptionally and post-transcriptionally. However, these processes can be independent of each other as in the case of pRip1 overproduction.

To assess if the Hsp42 and Hsp104 upregulation is associated with the response to protein aggregation (Balchin, Hayer-Hartl, & Hartl, 2016; Mogk, Kummer, & Bukau, 2015; Mogk, Ruger-Herreros, & Bukau, 2019), we evaluated if these chaperones recognize metastable mitochondrial protein aggregates. For that purpose, we labelled the FLAG-tagged metastable proteins with Alexa 568 fluorophore and followed its co-localisation with Hsp42-GFP by confocal microscopy. We observed a strong accumulation of pRip1 in the forms of large deposits in the cytosol (**Figure 3I**). These deposits co-localised with the GFP signals and indicated that Hsp42 sequestered pRip1 aggregates. If these specific chaperones were responsible for preventing aggregation of metastable proteins, we should observe a change in the amount of the accumulated proteins when they were not present in the cell. Indeed, in the cells with *hsp104* deletion, we observed an increased accumulation of the mitochondrial precursor protein pRip1 upon CCCP treatment (**Figure 3J**). Therefore, the Hsp104 function

bioRxiv preprint doi: https://doi.org/10.1101/2021.05.02.442342; this version posted May 2, 2021. The copyright holder for this preprint (which was not certified by peer review) is the author/funder, who has granted bioRxiv a license to display the preprint in perpetuity. It is made available under aCC-BY-NC-ND 4.0 International license.

was essential to limit aggregates of mitochondrial precursors in the cytosol. To support this interpretation, we observed that Hsp104 protein came in the pellet fraction in higher amount than when compared to the soluble fraction in our aggregation assay, suggesting that Hsp104 bound present there aggregates (**Figure 3K**).

Mitochondrial failure impairs cellular protein homeostasis

Furthermore, we asked whether the presence of metastable and aggregation-prone mitochondrial precursors could initiate the accumulation of precursor forms of other mitochondrial proteins. We verified that this is the case for some of the studied here metastable proteins. The overproduction of Atp2, Cox8 resulted in the concurrent accumulation of other mitochondrial protein, pRip1 and pSod2, in the total cell fractions, without any other stimulant than just overexpression of metastable proteins (**Figure 4A-C** and **Figure4–figure supplement 1A)**. The Atp20 overproduction also stimulated significant increase in the Sod2 precursor form in the total cell fractions, but not the pRip1 (**Figure 4A-C)**. The accumulated precursor proteins also co-aggregated with metastable proteins in the insoluble fraction based on the aggregation assay analysis (**Figure 4D,** and **Figure4–figure supplement 1B**). Thus, the increased abundance of aggregation-prone mitochondrial precursors resulted in progression of mitochondrial protein defects and as consequence deeper cytosolic aggregation of mitochondrial precursors. This observation might justify the reason why Atp2, Cox8, and Atp20 showed the most severe drop in lethality as presented by the drop-test results (**Figure 1B**). Moreover, this process was partially counteracted by proteasome-mediated degradation. MG132-mediated protein inhibition led to the increased accumulation and aggregation of mitochondrial precursor proteins (**Figure 4E,** and **Figure4–figure supplement 1C**).

bioRxiv preprint doi: https://doi.org/10.1101/2021.05.02.442342; this version posted May 2, 2021. The copyright holder for this preprint (which was not certified by peer review) is the author/funder, who has granted bioRxiv a license to display the preprint in perpetuity. It is made available under aCC-BY-NC-ND 4.0 International license.

Finally, we tested whether a chain reaction may take place, wherein the cytosolic aggregation of mitochondrial proteins at first impaired the import efficiency and solubility of other mitochondrial precursors, and subsequently induced the downstream aggregation of non-mitochondrial proteins. We used an established yeast model system of wild-type (WT) and A53T mutant of α-synuclein (α-Syn) tagged with the GFP (Outeiro & Lindquist, 2003). By the confocal microscopy experiments, we monitored the change in the average number of α-Syn aggregates per cell by following the signal of the GFP tag in response to the mitochondrial import. Here the mitochondrial defects were stimulated by the use of the temperature-sensitive *pam16-3* mutant. The average number of α-Syn aggregates per cell increased for *pam16-3* at a permissive temperature at 19 ˚C for both α-Syn WT-GFP and A53T-GFP when compared to the wild-type (**Figure 4F** and **4G,** and **Figure4–figure supplement 1D** and **1E**). The increase in average number of aggregates continued to grow for α-Syn WT-GFP at the restrictive 37 ˚C temperature (**Figure 4F**). The average number of α-Syn A53T-GFP formed aggregates was again higher at 37 ˚C than at the permissive temperature and did not significantly increase upon mitochondrial import defect in *pam16-3* mutant (**Figure 4G**). This observation might be justified by the difference in the properties of WT and A53T α-Syn aggregates. A53T mutations of α-Syn results in the aggregates bigger in size, when compared to the WT (Outeiro & Lindquist, 2003). The A53T α-Syn puncta were bigger and better resolved than the WT α-Syn (**Figure 4G**). We hypothesised that in case of A53T α-Syn at 37 ˚C, the number of average aggregates did not change significantly after reaching some threshold and instead they got bigger in size. Interestingly, we observed a higher accumulation of pRip at combined conditions of the *pam16-3* stimulated mitochondrial import defect and α-Syn aggregation at 37 ˚C (**Figure 4H** and **4I,** and **Figure4–figure supplement 1D and 1E**). Thus, the aggregation stimulation by the mitochondrial import defects had a two-sided effect: 1) α-Syn aggregation by itself was stimulated, and 2) α-Syn aggregations further deepened the aggregation of mitochondrial

bioRxiv preprint doi: https://doi.org/10.1101/2021.05.02.442342; this version posted May 2, 2021. The copyright holder for this preprint (which was not certified by peer review) is the author/funder, who has granted bioRxiv a license to display the preprint in perpetuity. It is made available under aCC-BY-NC-ND 4.0 International license.

precursor proteins. These results indicated that mitochondrial precursor aggregation in the cytosol led to increased aggregation of other non-mitochondrial proteins, and this snowball effect of proteins aggregation caused a reduced cellular protein homeostasis.

Next, to assess whether mitochondrial precursor aggregation due to mitochondrial protein import deficiency compromised protein homeostasis at an organismal level, we used *C. elegans* as a model system. For this purpose, we utilised RNAi silencing *dnj-21* (a homolog of yeast Pam18) strain in *C. elegans*, which stimulated mitochondrial import defect similar to the one observed in yeast for *pam16-3*. RNAi silencing of *dnj-21* in the early adulthood of *C. elegans*, was sufficient to stimulate the cytosolic aggregation of the RFP and GFP (**Figure 5A-C** and **Figure5–figure supplement 1A**). Next, we tested if the changes of the cellular homeostasis due to mitochondrial defects affected the health state of *C. elegans*, which produced α-Syn. Interestingly, the *dnj-21* silencing accompanied by α-Syn expression resulted in the reduced fitness of worms, manifested by a decrease in movement speed and fewer bends when compared to the effect of *dnj-21* silencing alone (**Figure 5D**). Finally, we assessed if the link between mitochondrial dysfunction was only limited to α-Syn, or similar effects could be observed for other proteins linked to neurodegeneration. For that purpose, we asked the question whether mitochondrial dysfunction would enhance amyloid β (Aβ) aggregation in the worms. We used animals carrying Aβ amyloids in body wall muscles and demonstrating paralysis behaviour in adults when shifted to 25 ˚C **(Figure5–figure supplement 1B**) (Sorrentino et al., 2017). The number of Aβ aggregates was elevated at 22 ˚C when *dnj-21* was silenced (**Figure 5E and 5F** and **Figure5–figure supplement 1C)**. This stimulated aggregation was a result of mitochondrial import defect without any accompanying changes in the expression of Aβ peptides (**Figure5–figure supplement 1D** and **1E**). We discovered that Aβ aggregation was accompanied by the decreased motility of *dnj-21* RNAi silenced worms (**Figure 5G,** and **Figure5–figure supplement 1F**). Our results showed that the mechanism of

bioRxiv preprint doi: https://doi.org/10.1101/2021.05.02.442342; this version posted May 2, 2021. The copyright holder for this preprint (which was not certified by peer review) is the author/funder, who has granted bioRxiv a license to display the preprint in perpetuity. It is made available under aCC-BY-NC-ND 4.0 International license.

aggregation stimulation due to mitochondrial dysfunction was conserved between the species, as we demonstrated for both α-Syn and Aβ amyloids.

Discussion

In this study, we have shown that a group of mitochondrial proteins downregulated in Alzheimer's disease, including Atp2, Cox8, and Atp20, can aggregate in the cytosol, and that the overexpression of these proteins causes the upregulation of the Hsp42 and Hsp104 chaperones, which are responsible for the recognition and management of protein aggregates (Balchin et al., 2016; Mogk et al., 2015; Mogk et al., 2019). This regulation, which we found to be stimulated only post-transcriptionally, adds to the known transcriptomic response mechanisms to mitochondrial import machinery overloading (Boos et al., 2019). Stress responses induced by mitochondrial proteins, such as the one identified here, reduce the danger related to aberrant formation of aggregates by mitochondrial metastable proteins.

Our study has also demonstrated that the mitochondrial import defects, either triggered chemically or with use of mutations of the TIM23 translocase, resulted in the accumulation and aggregation of mitochondrial precursor proteins. Consistently with experiments utilizing overproduction of metastable mitochondrial proteins, a Hsp42 and Hsp104 specific molecular chaperone response was also triggered in the cell with mitochondrial import defects. In addition, the ubiquitin proteasome system (UPS) could mitigate this process to some extent (Wrobel et al., 2015).

The unresolved aggregation of mistargeted metastable mitochondrial proteins eventually resulted in a chain reaction leading to the accumulation of deposits formed by other non-mitochondrial proteins. The collapse of cellular homeostasis resulted in the increase of pRip1 and α-Syn aggregation when the mitochondrial import was impaired. More generally, we found that an increased aggregation of proteins linked to age-related degenerations under

bioRxiv preprint doi: https://doi.org/10.1101/2021.05.02.442342; this version posted May 2, 2021. The copyright holder for this preprint (which was not certified by peer review) is the author/funder, who has granted bioRxiv a license to display the preprint in perpetuity. It is made available under aCC-BY-NC-ND 4.0 International license.

the conditions of mitochondrial protein import dysfunction was a conserved cellular mechanism that we observed it both in yeast and *C. elegans*. We demonstrated that aggregation of α-Syn and Aβ increased due to mitochondrial dysfunction on the organismal level, and was accompanied by the decrease of worm fitness.

Recently, several stress response pathways have been identified to counteract the defects of mitochondrial protein import (Boos et al., 2019; Wang & Chen, 2015; Weidberg & Amon, 2018; Wrobel et al., 2015). It has not been fully understood, however, if they act independently, or the concurrent action of all of them is needed to secure balanced cellular protein homeostasis. In our case, the MitoCPR complemented the chaperone response at the later stage of mitochondrial protein import impairment. Therefore, our results indicate that mitoprotein-induced stress responses are orchestrated to complement each other.

Overall, we observed an aggregation snowball effect when rescue mechanisms against aberrant aggregation, including the action of molecular chaperones, are not sufficient to control it. Our findings led to a model in which a cascade of events triggered by the cytosolic aggregation of specific metastable mitochondrial proteins contributes to the collapse of the cellular protein homeostasis and primes the aggregation of other proteins, including some linked to age-related degeneration. Consequently, defects in mitochondrial function, which are commonly observed upon ageing and in neurodegeneration, triggered a vicious cycle of protein aggregation. This notion is essential for understanding cellular events that contribute to the onset and progression of neurodegenerative processes. Overall, our results illustrate an important aspect of the interdependence of the mitochondrial fitness and cellular protein homeostasis systems, with direct relevance for common neurodegenerative disorders and mitochondrial function. Thus, our findings may suggest new avenues for therapeutic interventions to cure or prevent the diseases linked to protein misfolding and aggregation.

bioRxiv preprint doi: https://doi.org/10.1101/2021.05.02.442342; this version posted May 2, 2021. The copyright holder for this preprint (which was not certified by peer review) is the author/funder, who has granted bioRxiv a license to display the preprint in perpetuity. It is made available under aCC-BY-NC-ND 4.0 International license.

Materials and methods

Experimental Design. No statistical methods were used to predetermine sample size. The experiments were not randomized. The investigators were not blinded to allocation during experiments and outcome assessment. All experiments were repeated in at least 3 biological replicates.

Yeast strains. *Saccharomyces cerevisiae* strains are derivatives of YPH499 (MATa, ade2-101, his3-D200, leu2-D1, ura3-52, trp1-D63, lys2-801) or BY4741 (MATa, his3D1; leu2D0; met15D0; ura3D0). Wild-type yeast cells description refers to the BY4741 strain, if not otherwise stated. For the inducible expression of FLAG-tagged metastable proteins, the amino acid sequences were amplified by polymerase chain reaction (PCR) from yeast genomic DNA. The resulting DNA fragments were cloned in frame with the FLAG tag with use of the oligonucleotides indicated in **Supplementary file 1** into the pESC-URA vector (Agilent) where the GAL10 and GAL1 promoters were replaced with the Cup1 promoter. This procedure yielded the pPCh17 (481p), pPCh18 (482p), pPCh19 (484p), pPCh20 (485p), pPCh21 (486p), pPCh22 (487p), pPCh23 (488p), pPCh24 (489p), pPCh26 (492p), pPCh29 (490p), pPCh30 (483p), pPB36.1 (471p)(Kowalski et al., 2018) plasmids, with a FLAG tag at the C-terminus and expressed under the control of the Cup1 promoter (**Supplementary file 2**). Yeast cells were transformed according to the standard procedure. The *Δhsp104* deletion yeast stains was bought from Euroscarf. The *hsp42-GFP* yeast strain was bought from Invitrogen. The temperature-sensitive *pam16-1* (YPH-BG-mia1-1; 733), *pam16-3* (YPH-BGmia1-3; 734), with corresponding wild-type, *pam16-WT* (736) were described previously (Frazier et al., 2004). The temperature-sensitive *pam18-1* (YPH-BG-Mdj3-66; 739) with respective wild-type, *pam18-WT* (738) was described before (Truscott et al., 2003); similarly, as *mia40-3* (YPH-

bioRxiv preprint doi: https://doi.org/10.1101/2021.05.02.442342; this version posted May 2, 2021. The copyright holder for this preprint (which was not certified by peer review) is the author/funder, who has granted bioRxiv a license to display the preprint in perpetuity. It is made available under aCC-BY-NC-ND 4.0 International license.

BGfomp2-8; 178), *mia40-4int*(305), and corresponding wild-type, *mia40-WT* (398) (Chacinska et al., 2004; Stojanovski et al., 2008).

Yeast growth, treatments, and analysis. In experiments where metastable proteins were overproduced the strains were grown on minimal synthetic medium (0.67% (w/v) yeast nitrogen base, 0.079% (w/v) complete supplement mixture (CSM) amino acid mix, without uracil containing 2% (w/v) glucose or 2% (w/v) sucrose as carbon source. The yeast culture was carried at 28 °C to the early logarithmic growth phase and were further induced with 100 µM $CuSO_4$ for 4 h, if not otherwise stated. For the CCCP (Sigma C2759) treatment experiments, yeast strains were grown in the full medium containing 2% (w/v) glucose or 2% (w/v) sucrose at 24 °C, to the early logarithmic growth phase at which they were treated with 0, 5, 10 or 15 µM for 15 or 30 min at the growth temperature. The temperature-sensitive mutants were grown at permissive temperature 19 ^{o}C and analysed with or without-a shift to a restrictive temperature of 37 ^{o}C for the indicated time. The temperature-sensitive *pam16-3* mutants, which were transformed with the p426 α-Syn WT-GFP or A53T-GFP plasmids with galactose induction, were grown at permissive temperature 19 ^{o}C to the early logarithmic growth phase. Next, they were further induced with 0.5% (w/v) galactose for another 4 h. After the induction sample were shifted to the restrictive temperate of 37 ^{o}C for the heat shock, or left at 19 ^{o}C as a control for 2 h. The p426 GAL α-Syn WT-GFP or A53T-GFP were a gift from Dr. Tiago Outeiro (Göttingen). In experiments, where proteasome inhibition was used, the strains were grown on minimal synthetic medium (0.67% (w/v) yeast nitrogen base, 0.079% (w/v) CSM amino acid mix without ammonium sulfate supplemented with 0.1% (w/v) proline, 0.03% (w/v) SDS and 2% (w/v) galactose as carbon source at permissive 19 °C to the early logarithmic growth phase. Then, 75 µM MG132 was added to the cell culture and maintained at 19 ^{o}C or transferred to a restrictive temperature of 37 ^{o}C for indicated time. Proteins were separated by SDS-PAGE

bioRxiv preprint doi: https://doi.org/10.1101/2021.05.02.442342; this version posted May 2, 2021. The copyright holder for this preprint (which was not certified by peer review) is the author/funder, who has granted bioRxiv a license to display the preprint in perpetuity. It is made available under aCC-BY-NC-ND 4.0 International license.

using 12, or 15% gels, then transferred onto PVDF membranes. Immunodetection was performed according to standard techniques using chemiluminescence. Following antibodies were used in the study: FLAG (Sigma, Cat. No. F1804), GFP (Sigma, Cat. No. 11814460001), Hsp104 (Enzo, Cat. No. ADI-SPA-1040-F), Alexa Fluor 568 (Invitrogen, Cat. No. A11031), Rip1, Sod2, Mdh1, Hsp60, Pgk1, Tom70, Ssa1, Ssc1, Rpl17, Ccp1, Qcr8, Qcr6, Cox12, Tom20, Ssb1, Edg1, Cdc48, Rpl5, DNJ-21 are noncommercial antibodies and are available in the laboratory depository.

Aggregation assay. 10 OD_{600} units of cells were harvested by centrifugation (5000 g, 5 min, 4 °C) and re-suspended in 400 µl of Lysis buffer (30 mM Tris-HCl pH 7.4, 20 mM KCl, 150 mM NaCl, 5 mM EDTA, 0,5 mM PMSF). Cells were homogenized by vortexing with 200 µl of glass beads (425–600 µm, Sigma-Aldrich) using a Cell Disruptor Genie (Scientific Industries) for 10 min at 4 °C. Cell lysate was solubilized with 1% [v/v] Triton X-100 and mixed gently for 20 min at 4 °C. The sample was centrifuged (4000 g, 5 min, 4 °C) to remove unbroken cells and detergent-resistant aggregates (P_{4k}). Next, the supernatant was transferred into two tubes at equal volumes. One was saved as total protein fraction (T). Second sample was centrifuged (125,000 g, 60 min, 4 °C) to separate soluble proteins (S_{125k}) from protein aggregates (P_{125k}). Total (T) and soluble (S_{125k}) fractions were precipitated by 10% trichloroacetic acid. After 30 min incubation on ice the samples were centrifuged (20000 g, 15 min, 4 °C), washed with ice-cold acetone and centrifuged again. The obtained pellets from T and S_{125k} sample as well as P_{4k} and P_{125k} were re-suspended in urea sample buffer (6 M urea, 6 % [w/v] SDS, 125 Tris-HCl pH 6.8, 0.01% [w/v] bromophenol blue, incubated for 15 min at 37 °C and analysed by SDS-PAGE followed by western-blotting.

RNA-seq – sample preparation

bioRxiv preprint doi: https://doi.org/10.1101/2021.05.02.442342; this version posted May 2, 2021. The copyright holder for this preprint (which was not certified by peer review) is the author/funder, who has granted bioRxiv a license to display the preprint in perpetuity. It is made available under aCC-BY-NC-ND 4.0 International license.

The total RNA was isolated from *pam16-3* mutant and corresponding wild-type samples, as well as, BY4741 cells transformed with pESC-URA plasmid expressing pRIp1-FLAG protein or empty vector under the control of the Cup1 promoter. The pRip1 related samples were grown at 28 °C to the early logarithmic growth phase and were further induced with 100 µM CuSO4 for 1, 4 or 8 h. *Pam16* wild-type and the mutant *pam16-3* sample after growing to the early logarithmic phase and were shifted to a restrictive temperature of 37 °C for 0, 1, 4 or 8 h. 2.5 OD600 units of cells were harvested by centrifugation (5000 g, 5 min, 4 °C), re-suspended in 125 µl of RNAlater solution (Thermo Fisher Scientific, AM7020) and incubated for 1 h at 4 °C. After re-centrifugation, the cell pellet was frozen in liquid nitrogen and stored for further processing.

The *pam16-3* and pRip1 related samples for RNA sequencing were prepared including four biological replicates. Each replicate was individually generated from frozen stocks. The defrost samples were spun at 5000 g for 5 min at 4 °C to remove thoroughly the supernatants. The loosen pellet were re-suspend in 200 uL PBS. To this sample, 600 uL of Buffer RLT (Qiagen Cat No./ID: 79216) was added along with acid-washed glass beads, and cells were shaken in a cell disruptor for 10 min at max speed at 4 °C. The further processing was performed with agreement of the RNA extraction from Qiagen Purification of Total RNA Kit for Yeast with Optimal On-Column DNase Digestion (RNeasy Mini Kit (50), Qiagen Cat No./ID: 74104).

RNA-seq – analysis

Sequencing was performed on the Illumina NextSeq500 instrument using v2 chemistry, resulting in average of 15-20 M reads per library with 75 bp single end setup. The resulting raw reads were assessed for quality, adapter content, and duplication rates with FastQC (Andrews, 2010). Reads for each sample were aligned versus the Ensembl *Saccharomyces cerevisiae* transcriptome version 91 (Saccharomyces_cerevisiae.R64-1-1.91.gtf) and quantified using

bioRxiv preprint doi: https://doi.org/10.1101/2021.05.02.442342; this version posted May 2, 2021. The copyright holder for this preprint (which was not certified by peer review) is the author/funder, who has granted bioRxiv a license to display the preprint in perpetuity. It is made available under aCC-BY-NC-ND 4.0 International license.

Salmon (v0.11.2) (Patro, Duggal, Love, Irizarry, & Kingsford, 2017) with default parameters. Full lists of genes for *pam16-3* and pRip1 samples are available in **Figure2-Source Data 1 and Figure2-Source Data 2**, respectively. Expression matrices for *pam16-3 a*nd pRip1 strains are available in **Figure2-Source Data 3** and **Figure2-Source Data 4**, respectively. For each time point, differentially expressed genes were identified using DESeq2 (Love, Huber, & Anders, 2014) version 1.26.0. Only genes with a minimum fold change of log2 +/-1, a maximum Benjamini-Hochberg corrected P-value of 0.05, and a minimum combined mean of 10 reads were deemed to be significantly differentially expressed. The wild-type samples were used as a reference in *pam16-3*, while samples with empty pESC-URA plasmid were control in pRip1 comparisons. Raw data were deposited to GEO repository with the accession number GSE147284. Raw data are available at https://www.ncbi.nlm.nih.gov/geo/query/acc.cgi?acc=GSE147284 using the token: mvwtuqeexrgvbut.

KEGG enrichment analysis

Kyoto Encyclopedia of Genes and Genomes (KEGG) enrichment analysis was performed for RNA sequencing using in house developed methods based on KEGG.db (v. 3.2.3) and org.SC.sgd.db (v 3.10.0). Pathways and genes selected in each developmental stage were filtered after Benjamini-Hochberg correction for an adjusted P-value < 0.05.

Microscopy. Yeast confocal microscopy images of GAL α-Syn WT-GFP or A53T-GFP in *pam16-3* mutant and its corresponding wild-type were acquired with a Zeiss LSM700 laser-scanning confocal microscope using a 60x oil objective (NA 1.4). Images were recorded with pixel dimensions of 25 nm. To investigate the presence and distribution of aggregates, we used 2 photomultiplier tube (PMT) detectors with the 405 nm laser excitation for DAPI and the 488

bioRxiv preprint doi: https://doi.org/10.1101/2021.05.02.442342; this version posted May 2, 2021. The copyright holder for this preprint (which was not certified by peer review) is the author/funder, who has granted bioRxiv a license to display the preprint in perpetuity. It is made available under aCC-BY-NC-ND 4.0 International license.

nm for the GFP fluorescence scanned sequentially. The yeast cells were visualized using 1AU confocal pinhole and many z-stacks (typically between 20-25) were acquired, each with optical thickness of 0.28 µm. The cytosolic aggregates were counted manually from the z-stacks Maximum Intensity Projection merge. The metastable co-localisation experiments in the *hsp42-GFP* strain were performed as above, with the additional detection of metastable proteins through immunofluorescence. Metastable proteins were labelled through the standard immunofluorescence protocol, with 1:1000 concentration of the FLAG antibody (Sigma, F1804), and the 1:500 secondary Alexa Fluor 568 antibody (Invitrogen, A11031). To analyse the number of RFP and GFP aggregates in *C. elegans* we recorded fluorescence images of the head region of worms expressing wrmScarlet (RFP) and GFP in body wall muscles (strain ACH87). Pictures were captured with the usage of Zeiss 700 laser-scanning confocal microscope using a 40x oil objective (NA 1.3). To investigate the presence and distribution of aggregates, we used 2 PMT detectors with the 488 nm laser excitation for GFP and the 555 nm for the RFP fluorescence scanned sequentially. Worms head regions were visualized using 1AU confocal pinhole and a number of z-stacks (typically between 35-45) were acquired, each with optical thickness of 1 µm. 8 to 15 animals were taken per condition, per each day of worms' adulthood, starting from L4 larvae as day 0 until day 5 of adulthood. Next, z-stacks were merged using Maximum Intensity Projection. Finally, RFP and GFP aggregates were extracted from pictures and counted in an automatic way with the usage of ImageJ. For all microscopy experiments the exposure parameters were chosen that way that no saturation effect for the fluorescent signal was present, and kept on the same level during the whole experiment.

Co-localisation analysis. Fluorescence co-localisation between the Alexa568 FLAG (red channel) and the Hsp42-GFP (green channel) was calculated on individual yeast cells, 3 cells per conditions (marked as individual regions of interest (ROIs)), in a form of Pearson's

bioRxiv preprint doi: https://doi.org/10.1101/2021.05.02.442342; this version posted May 2, 2021. The copyright holder for this preprint (which was not certified by peer review) is the author/funder, who has granted bioRxiv a license to display the preprint in perpetuity. It is made available under aCC-BY-NC-ND 4.0 International license.

correlation coefficients above Costes threshold using the Co-localisation Threshold plugin of ImageJ. This was followed by running the Co-localisation Test plugin of ImageJ to test statistical significance of the performed calculations. A resulting P-values of 1.00 indicated the results to be statistically significant.

Worm maintenance and strains. Standard conditions were used for the propagation of *C. elegans* (Brenner, 1974). Briefly, the animals were synchronized by hypochlorite bleaching, hatched overnight in M9 buffer (3 g/L KH_2PO_4, 6 g/L Na_2HPO_4, 5 g/L NaCl, 1 M $MgSO_4$), and subsequently cultured at 20 °C on nematode growth medium (NGM) plates (1 mM $CaCl_2$, 1 mM $MgSO_4$, 5 µg/mL cholesterol, 25 mM KPO_4 (buffer (pH 6.0), 17 g/L Agar, 3 g/L NaCl, 2.5 g/L peptone) seeded with the *E. coli* strain HB101 or OP50 as a food source. Following *C. elegans* strains were used:

CL2122: dvIs15 [(pPD30.38) unc-54(vector) + (pCL26) mtl-2::GFP]. Control strain for GMC101.

GMC101: dvIs100 [punc-54::A-beta-1-42::unc-54-3'-UTR + mtl-2p::GFP]

ACH87: wacIs11 [pmyo-3::mGFP::SL2 gdp-2-wrmScarlet::unc-54-3’UTR, unc-119(+)]

OW40: zgIs15 [punc-54::αsyn::YFP]IV (van Ham et al., 2008)

OW450: rmIs126 [punc-54::YFP]V. Control strain for OW40 (van Ham et al., 2008)

Molecular biology for worms studies. A RNAi construct targeting the *dnj-21* gene was created by PCR amplification of gene from cDNA pools generated from RNA. Primers used for generating PCR product were designed to amplify full cDNA sequence of *dnj-21*. The PCR product was digested with XhoI and KpnI restriction enzymes and cloned into the XhoI and KpnI-digested L4440 vector. Construct for expression of wrmScarlet (RFP – mCherry derivative) (El Mouridi et al., 2017) and mGFP in the body wall muscles of the worms was

bioRxiv preprint doi: https://doi.org/10.1101/2021.05.02.442342; this version posted May 2, 2021. The copyright holder for this preprint (which was not certified by peer review) is the author/funder, who has granted bioRxiv a license to display the preprint in perpetuity. It is made available under aCC-BY-NC-ND 4.0 International license.

created with usage of SLiCE method (Zhang, Werling, & Edelmann, 2012) and the Three Fragment Gateway System (Invitrogen, Carlsbad, CA). Briefly, wrmScarlet from plasmid pSEM87 was PCR amplified with the usage of following primers: ggaaactgcttcaacgcatcatggtcagcaagggagag and gaagagtaattggacttacttgtagagctcgtccatt. PCR product was used for replacement of mKate2 sequence in pCG150 vector with pmyo-3::mGFP::SL2 gdp-2-mKate2::unc-54-3'UTR insert. Cloned constructs were sequenced for inserts verification.

Worms transformation. The *C. elegans* transgenic strain ACH87 was created with the usage of biolistic bombardment as described before (Praitis, Casey, Collar, & Austin, 2001). The *unc-119* rescue was used as a selection marker.

Worms RNA interference (RNAi). RNAi was achieved by feeding worms with *E. coli* HT115(DE3) bacteria transformed with construct targeting the *dnj-21* gene. *E. coli* HT115(DE3) transformed with empty vector L4440 was used as a control. LB medium (10 g/L tryptone, 10 g/L NaCl, 5 g/L yeast extract) was inoculated with transformed bacteria and cultured in 37 ˚C, 180 RPM. Bacterial culture was induced with 1 mM IPTG once culture OD_{600} reached 0.4 – 0.6. After 2 h bacteria were pelleted. For liquid culture, bacterial pellet was added to S-medium and used for further worm culture. For culture on solid medium, plates were seeded with bacteria and used after bacteria have dried.

Worms total protein isolation and western blot. GMC101 L1 larvae were cultured in liquid S-medium for 3 days for 24 h at 20 ˚C and then the temperature was maintained at 20 ˚C or increased to 22 ˚C or 25 ˚C for 48 h to induce Aβ aggregation. Total proteins were isolated from frozen worm pellets. Samples were thawed on ice in lysis buffer (20 mM Tris pH 7.4, 200 mM

bioRxiv preprint doi: https://doi.org/10.1101/2021.05.02.442342; this version posted May 2, 2021. The copyright holder for this preprint (which was not certified by peer review) is the author/funder, who has granted bioRxiv a license to display the preprint in perpetuity. It is made available under aCC-BY-NC-ND 4.0 International license.

NaCl, 2mM PMSF) and sonicated 3 times for 10 s. The lysate was centrifuged at 2800 g, 5 min, 4 ˚C. The pellet containing debris was discarded. Protein concentration was measured with DirectDetect. Proteins were separated by SDS-PAGE (using 15% gels) or native PAGE (12% gels), then transferred onto PVDF membranes. Immunodetection was performed according to standard techniques using chemiluminescence. The following antibodies were used: custom-made rabbit antibody against DNJ-21, Purified anti-β-Amyloid 1-16 Antibody (803001 Biolegend), Tubulin (T9026, Sigma), mCherry (ab167453, abcam), GFP (11814460001, Sigma).

Motility assay. Animals were placed in a drop of M9 buffer and allowed to recover for 30 s to avoid the observation of behaviour associated with stress, after which the number of body bends was counted for 30 s. The experiments were carried out in triplicates and for each experiment at least 35 animals were analysed in total.

Automated body bend assay. Automated motility assessment was performed with tracking device developed and described previously (Perni et al., 2018). Shortly, worms were washed off the plates with M9 buffer and spread over 9 cm NGM plate in a final volume of 5 mL, after which their movements were recorded for 120 s. Videos were analysed in a consistent manner to track worm motility (bends per minute) and speed of swimming. The results show average from two independent experiments ± SEM.

Statistical analysis: For statistical analysis, a two-tailed, unpaired t-test was used assuming equal variance unless otherwise stated. P-value ≤ 0.05 was considered significant. For the statistical analysis of the confocal microscopy co-localisation data please refer also to the co-localisation analysis section of the Methods.

bioRxiv preprint doi: https://doi.org/10.1101/2021.05.02.442342; this version posted May 2, 2021. The copyright holder for this preprint (which was not certified by peer review) is the author/funder, who has granted bioRxiv a license to display the preprint in perpetuity. It is made available under aCC-BY-NC-ND 4.0 International license.

Data and materials availability: The authors declare that the data supporting the findings of this study are available within the paper, supporing information and source data.

Acknowledgments

We thank Tiago Outeiro, Henrik Bringmann, Thomas Boulin, Ellen Nollen and Agnieszka Sztyler for materials and experimental assistance and CGC, funded by NIH Office of Research Infrastructure Programs (P40 OD010440) for providing *C. elegans* strains.

Author contributions: U.N., P.C., K.S., M.S., M.T., T.G. and M.P. performed and analysed biochemical experiments. U.N., P.C., K.S., B.U.R, and R.K. performed RNA-seq and analyses. C.M.D., M.V., and A.C. conceived the project. All authors interpreted the experiments. M.V. and A.C. analysed and supervised the study. U.N, M.V. and A.C. wrote the manuscript with the input of other authors.

Competing interests: The authors declare no competing financial interests.

References

Andreasson, C., Ott, M., & Buttner, S. (2019). Mitochondria orchestrate proteostatic and metabolic stress responses. *EMBO Rep*, *20*(10), e47865. doi:10.15252/embr.201947865

bioRxiv preprint doi: https://doi.org/10.1101/2021.05.02.442342; this version posted May 2, 2021. The copyright holder for this preprint (which was not certified by peer review) is the author/funder, who has granted bioRxiv a license to display the preprint in perpetuity. It is made available under aCC-BY-NC-ND 4.0 International license.

Andrews, S. (2010). FastQC: a quality control tool for high throughput sequence data. Retrieved from http://www.bioinformatics.babraham.ac.uk/projects/fastqc

Balchin, D., Hayer-Hartl, M., & Hartl, F. U. (2016). In vivo aspects of protein folding and quality control. *Science, 353*(6294), aac4354. doi:10.1126/science.aac4354

Boos, F., Kramer, L., Groh, C., Jung, F., Haberkant, P., Stein, F., . . . Herrmann, J. M. (2019). Mitochondrial protein-induced stress triggers a global adaptive transcriptional programme. *Nat Cell Biol, 21*(4), 442-451. doi:10.1038/s41556-019-0294-5

Boos, F., Labbadia, J., & Herrmann, J. M. (2020). How the Mitoprotein-Induced Stress Response Safeguards the Cytosol: A Unified View. *Trends Cell Biol, 30*(3), 241-254. doi:10.1016/j.tcb.2019.12.003

Braun, R. J., & Westermann, B. (2017). With the Help of MOM: Mitochondrial Contributions to Cellular Quality Control. *Trends Cell Biol, 27*(6), 441-452. doi:10.1016/j.tcb.2017.02.007

Brenner, S. (1974). The genetics of Caenorhabditis elegans. *Genetics, 77*(1), 71-94.

Bruderek, M., Jaworek, W., Wilkening, A., Rub, C., Cenini, G., Fortsch, A., . . . Voos, W. (2018). IMiQ: a novel protein quality control compartment protecting mitochondrial functional integrity. *Mol Biol Cell, 29*(3), 256-269. doi:10.1091/mbc.E17-01-0027

Cabral-Costa, J. V., & Kowaltowski, A. J. (2020). Neurological disorders and mitochondria. *Mol Aspects Med, 71*, 100826. doi:10.1016/j.mam.2019.10.003

Calvo, S. E., Clauser, K. R., & Mootha, V. K. (2016). MitoCarta2.0: an updated inventory of mammalian mitochondrial proteins. *Nucleic Acids Res, 44*(D1), D1251-1257. doi:10.1093/nar/gkv1003

Cenini, G., Rub, C., Bruderek, M., & Voos, W. (2016). Amyloid beta-peptides interfere with mitochondrial preprotein import competence by a coaggregation process. *Mol Biol Cell, 27*(21), 3257-3272. doi:10.1091/mbc.E16-05-0313

bioRxiv preprint doi: https://doi.org/10.1101/2021.05.02.442342; this version posted May 2, 2021. The copyright holder for this preprint (which was not certified by peer review) is the author/funder, who has granted bioRxiv a license to display the preprint in perpetuity. It is made available under aCC-BY-NC-ND 4.0 International license.

Chacinska, A., Koehler, C. M., Milenkovic, D., Lithgow, T., & Pfanner, N. (2009). Importing mitochondrial proteins: machineries and mechanisms. *Cell, 138*(4), 628-644. doi:10.1016/j.cell.2009.08.005

Chacinska, A., Pfannschmidt, S., Wiedemann, N., Kozjak, V., Sanjuan Szklarz, L. K., Schulze-Specking, A., . . . Pfanner, N. (2004). Essential role of Mia40 in import and assembly of mitochondrial intermembrane space proteins. *EMBO J, 23*(19), 3735-3746. doi:10.1038/sj.emboj.7600389

Ciryam, P., Kundra, R., Freer, R., Morimoto, R. I., Dobson, C. M., & Vendruscolo, M. (2016). A transcriptional signature of Alzheimer's disease is associated with a metastable subproteome at risk for aggregation. *Proc Natl Acad Sci U S A, 113*(17), 4753-4758. doi:10.1073/pnas.1516604113

Claros, M. G., & Vincens, P. (1996). Computational method to predict mitochondrially imported proteins and their targeting sequences. *Eur J Biochem, 241*(3), 779-786.

Di Maio, R., Barrett, P. J., Hoffman, E. K., Barrett, C. W., Zharikov, A., Borah, A., . . . Greenamyre, J. T. (2016). alpha-Synuclein binds to TOM20 and inhibits mitochondrial protein import in Parkinson's disease. *Sci Transl Med, 8*(342), 342ra378. doi:10.1126/scitranslmed.aaf3634

El Mouridi, S., Lecroisey, C., Tardy, P., Mercier, M., Leclercq-Blondel, A., Zariohi, N., & Boulin, T. (2017). Reliable CRISPR/Cas9 Genome Engineering in Caenorhabditis elegans Using a Single Efficient sgRNA and an Easily Recognizable Phenotype. *G3 (Bethesda), 7*(5), 1429-1437. doi:10.1534/g3.117.040824

Escobar-Henriques, M., Altin, S., & Brave, F. D. (2020). Interplay between the Ubiquitin Proteasome System and Mitochondria for Protein Homeostasis. *Curr Issues Mol Biol, 35*, 35-58. doi:10.21775/cimb.035.035

bioRxiv preprint doi: https://doi.org/10.1101/2021.05.02.442342; this version posted May 2, 2021. The copyright holder for this preprint (which was not certified by peer review) is the author/funder, who has granted bioRxiv a license to display the preprint in perpetuity. It is made available under aCC-BY-NC-ND 4.0 International license.

Frazier, A. E., Dudek, J., Guiard, B., Voos, W., Li, Y., Lind, M., . . . Rehling, P. (2004). Pam16 has an essential role in the mitochondrial protein import motor. *Nat Struct Mol Biol, 11*(3), 226-233. doi:10.1038/nsmb735

Fukasawa, Y., Tsuji, J., Fu, S. C., Tomii, K., Horton, P., & Imai, K. (2015). MitoFates: improved prediction of mitochondrial targeting sequences and their cleavage sites. *Mol Cell Proteomics, 14*(4), 1113-1126. doi:10.1074/mcp.M114.043083

Gulshan, K., Schmidt, J. A., Shahi, P., & Moye-Rowley, W. S. (2008). Evidence for the bifunctional nature of mitochondrial phosphatidylserine decarboxylase: role in Pdr3-dependent retrograde regulation of PDR5 expression. *Mol Cell Biol, 28*(19), 5851-5864. doi:10.1128/MCB.00405-08

Izawa, T., Park, S. H., Zhao, L., Hartl, F. U., & Neupert, W. (2017). Cytosolic Protein Vms1 Links Ribosome Quality Control to Mitochondrial and Cellular Homeostasis. *Cell, 171*(4), 890-903 e818. doi:10.1016/j.cell.2017.10.002

Kim, H. E., Grant, A. R., Simic, M. S., Kohnz, R. A., Nomura, D. K., Durieux, J., . . . Dillin, A. (2016). Lipid Biosynthesis Coordinates a Mitochondrial-to-Cytosolic Stress Response. *Cell, 166*(6), 1539-1552 e1516. doi:10.1016/j.cell.2016.08.027

Kowalski, L., Bragoszewski, P., Khmelinskii, A., Glow, E., Knop, M., & Chacinska, A. (2018). Determinants of the cytosolic turnover of mitochondrial intermembrane space proteins. *BMC Biol, 16*(1), 66. doi:10.1186/s12915-018-0536-1

Kundra, R., Ciryam, P., Morimoto, R. I., Dobson, C. M., & Vendruscolo, M. (2017). Protein homeostasis of a metastable subproteome associated with Alzheimer's disease. *Proc Natl Acad Sci U S A, 114*(28), E5703-E5711. doi:10.1073/pnas.1618417114

Love, M. I., Huber, W., & Anders, S. (2014). Moderated estimation of fold change and dispersion for RNA-seq data with DESeq2. *Genome Biol, 15*(12), 550. doi:10.1186/s13059-014-0550-8

bioRxiv preprint doi: https://doi.org/10.1101/2021.05.02.442342; this version posted May 2, 2021. The copyright holder for this preprint (which was not certified by peer review) is the author/funder, who has granted bioRxiv a license to display the preprint in perpetuity. It is made available under aCC-BY-NC-ND 4.0 International license.

Martensson, C. U., Priesnitz, C., Song, J., Ellenrieder, L., Doan, K. N., Boos, F., . . . Becker, T. (2019). Mitochondrial protein translocation-associated degradation. *Nature, 569*(7758), 679-683. doi:10.1038/s41586-019-1227-y

Mogk, A., Kummer, E., & Bukau, B. (2015). Cooperation of Hsp70 and Hsp100 chaperone machines in protein disaggregation. *Front Mol Biosci, 2*, 22. doi:10.3389/fmolb.2015.00022

Mogk, A., Ruger-Herreros, C., & Bukau, B. (2019). Cellular Functions and Mechanisms of Action of Small Heat Shock Proteins. *Annu Rev Microbiol, 73*, 89-110. doi:10.1146/annurev-micro-020518-115515

Morgenstern, M., Stiller, S. B., Lubbert, P., Peikert, C. D., Dannenmaier, S., Drepper, F., . . . Warscheid, B. (2017). Definition of a High-Confidence Mitochondrial Proteome at Quantitative Scale. *Cell Rep, 19*(13), 2836-2852. doi:10.1016/j.celrep.2017.06.014

Mossmann, D., Vogtle, F. N., Taskin, A. A., Teixeira, P. F., Ring, J., Burkhart, J. M., . . . Meisinger, C. (2014). Amyloid-beta peptide induces mitochondrial dysfunction by inhibition of preprotein maturation. *Cell Metab, 20*(4), 662-669. doi:10.1016/j.cmet.2014.07.024

Neupert, W., & Herrmann, J. M. (2007). Translocation of proteins into mitochondria. *Annu Rev Biochem, 76*, 723-749. doi:10.1146/annurev.biochem.76.052705.163409

Outeiro, T. F., & Lindquist, S. (2003). Yeast cells provide insight into alpha-synuclein biology and pathobiology. *Science, 302*(5651), 1772-1775. doi:10.1126/science.1090439

Patro, R., Duggal, G., Love, M. I., Irizarry, R. A., & Kingsford, C. (2017). Salmon provides fast and bias-aware quantification of transcript expression. *Nat Methods, 14*(4), 417-419. doi:10.1038/nmeth.4197

bioRxiv preprint doi: https://doi.org/10.1101/2021.05.02.442342; this version posted May 2, 2021. The copyright holder for this preprint (which was not certified by peer review) is the author/funder, who has granted bioRxiv a license to display the preprint in perpetuity. It is made available under aCC-BY-NC-ND 4.0 International license.

Perni, M., Challa, P. K., Kirkegaard, J. B., Limbocker, R., Koopman, M., Hardenberg, M. C., . . . Knowles, T. P. J. (2018). Massively parallel C. elegans tracking provides multi-dimensional fingerprints for phenotypic discovery. *J Neurosci Methods, 306*, 57-67. doi:10.1016/j.jneumeth.2018.02.005

Pfanner, N., Warscheid, B., & Wiedemann, N. (2019). Mitochondrial proteins: from biogenesis to functional networks. *Nat Rev Mol Cell Biol, 20*(5), 267-284. doi:10.1038/s41580-018-0092-0

Praitis, V., Casey, E., Collar, D., & Austin, J. (2001). Creation of low-copy integrated transgenic lines in Caenorhabditis elegans. *Genetics, 157*(3), 1217-1226.

Priesnitz, C., & Becker, T. (2018). Pathways to balance mitochondrial translation and protein import. *Genes Dev, 32*(19-20), 1285-1296. doi:10.1101/gad.316547.118

Ruan, L., Zhou, C., Jin, E., Kucharavy, A., Zhang, Y., Wen, Z., . . . Li, R. (2017). Cytosolic proteostasis through importing of misfolded proteins into mitochondria. *Nature, 543*(7645), 443-446. doi:10.1038/nature21695

Sormanni, P., Aprile, F. A., & Vendruscolo, M. (2015). The CamSol method of rational design of protein mutants with enhanced solubility. *J Mol Biol, 427*(2), 478-490. doi:10.1016/j.jmb.2014.09.026

Sorrentino, V., Romani, M., Mouchiroud, L., Beck, J. S., Zhang, H., D'Amico, D., . . . Auwerx, J. (2017). Enhancing mitochondrial proteostasis reduces amyloid-beta proteotoxicity. *Nature, 552*(7684), 187-193. doi:10.1038/nature25143

Stojanovski, D., Milenkovic, D., Muller, J. M., Gabriel, K., Schulze-Specking, A., Baker, M. J., . . . Chacinska, A. (2008). Mitochondrial protein import: precursor oxidation in a ternary complex with disulfide carrier and sulfhydryl oxidase. *J Cell Biol, 183*(2), 195-202. doi:10.1083/jcb.200804095

bioRxiv preprint doi: https://doi.org/10.1101/2021.05.02.442342; this version posted May 2, 2021. The copyright holder for this preprint (which was not certified by peer review) is the author/funder, who has granted bioRxiv a license to display the preprint in perpetuity. It is made available under aCC-BY-NC-ND 4.0 International license.

Truscott, K. N., Voos, W., Frazier, A. E., Lind, M., Li, Y., Geissler, A., . . . Pfanner, N. (2003). A J-protein is an essential subunit of the presequence translocase-associated protein import motor of mitochondria. *J Cell Biol, 163*(4), 707-713. doi:10.1083/jcb.200308004

van der Laan, M., Hutu, D. P., & Rehling, P. (2010). On the mechanism of preprotein import by the mitochondrial presequence translocase. *Biochim Biophys Acta, 1803*(6), 732-739. doi:10.1016/j.bbamcr.2010.01.013

van Ham, T. J., Thijssen, K. L., Breitling, R., Hofstra, R. M., Plasterk, R. H., & Nollen, E. A. (2008). C. elegans model identifies genetic modifiers of alpha-synuclein inclusion formation during aging. *PLoS Genet, 4*(3), e1000027. doi:10.1371/journal.pgen.1000027

Vecchi, G., Sormanni, P., Mannini, B., Vandelli, A., Tartaglia, G. G., Dobson, C. M., . . . Vendruscolo, M. (2020). Proteome-wide observation of the phenomenon of life on the edge of solubility. *Proc Natl Acad Sci U S A, 117*(2), 1015-1020. doi:10.1073/pnas.1910444117

Vicario, M., Cieri, D., Brini, M., & Cali, T. (2018). The Close Encounter Between Alpha-Synuclein and Mitochondria. *Front Neurosci, 12*, 388. doi:10.3389/fnins.2018.00388

Wang, X., & Chen, X. J. (2015). A cytosolic network suppressing mitochondria-mediated proteostatic stress and cell death. *Nature, 524*(7566), 481-484. doi:10.1038/nature14859

Weidberg, H., & Amon, A. (2018). MitoCPR-A surveillance pathway that protects mitochondria in response to protein import stress. *Science, 360*(6385). doi:10.1126/science.aan4146

bioRxiv preprint doi: https://doi.org/10.1101/2021.05.02.442342; this version posted May 2, 2021. The copyright holder for this preprint (which was not certified by peer review) is the author/funder, who has granted bioRxiv a license to display the preprint in perpetuity. It is made available under aCC-BY-NC-ND 4.0 International license.

Wrobel, L., Topf, U., Bragoszewski, P., Wiese, S., Sztolsztener, M. E., Oeljeklaus, S., . . . Chacinska, A. (2015). Mistargeted mitochondrial proteins activate a proteostatic response in the cytosol. *Nature, 524*(7566), 485-488. doi:10.1038/nature14951

Wu, Z., Tantray, I., Lim, J., Chen, S., Li, Y., Davis, Z., . . . Lu, B. (2019). MISTERMINATE Mechanistically Links Mitochondrial Dysfunction with Proteostasis Failure. *Mol Cell, 75*(4), 835-848 e838. doi:10.1016/j.molcel.2019.06.031

Zhang, Y., Werling, U., & Edelmann, W. (2012). SLiCE: a novel bacterial cell extract-based DNA cloning method. *Nucleic Acids Res, 40*(8), e55. doi:10.1093/nar/gkr1288

bioRxiv preprint doi: https://doi.org/10.1101/2021.05.02.442342; this version posted May 2, 2021. The copyright holder for this preprint (which was not certified by peer review) is the author/funder, who has granted bioRxiv a license to display the preprint in perpetuity. It is made available under aCC-BY-NC-ND 4.0 International license.

Figure Legends

Figure 1. Supersaturated nuclear-encoded mitochondrial proteins aggregate in the cytosol. (**A**) SDS-PAGE analysis of the aggregation assays fractions of the wild-type yeast cells overexpressing $Atp2_{FLAG}$, $Atp20_{FLAG}$, $Cox8_{FLAG}$, $pRip1_{FLAG}$, $Qcr8_{FLAG}$, $Cor1_{FLAG}$, $Mas1_{FLAG}$, $Cox12_{FLAG}$ and $Qcr6_{FLAG}$ for 3 h. Pellet fractions after 4k and 125k speed spin are indicated as P_{4k} and P_{125k}, respectively, the soluble fraction at 125k as S_{125k}. (**B**) Tenfold dilutions of wild-type cells expressing metastable proteins, or controls spotted on selective medium agar plates with galactose as the main carbon source at 28 °C and 37 °C. (**C**) Total protein cell extract from wild-type yeast grown at 24 °C and treated with 0, 5, 10, or 15 µM CCCP for 30 min. (**D**) Quantification of pRip1, pSod2, and pMdh1 froms from (C). Quantified data are mean ± SEM, for n=3. (**E**) SDS-PAGE analysis of the aggregation assay fractions of the yeast cells treated with 15 µM CCCP for 30 min . (**F**) SDS-PAGE analysis of the aggregation assay fractions of wild-type (WT) and *pam16-3* mutant yeast strains grown at 19 °C and shifted to 37 °C for 0, 3, or 5 h. In (A, C, E, F), samples were separated by SDS-PAGE and identified by western-blotting with specific antisera. p-presequence protein, i-intermediate protein, m-mature protein, *-not specific, Significance: * p-value<0.05, ** p-value≤0.01; *** p-value≤0.001; **** p≤0.0001.

Figure supplement 1. Aggregation propensity characterisation of mitochondrial proteins.

Figure supplement 2. Supersaturated nuclear-encoded mitochondrial proteins aggregate in the cytosol and stimulate growth defects..

Figure 2. Mitochondrial protein import defects stimulate specific transcriptomic responses. (**A, B**) Volcano plot comparing expression changes (in terms of the logarithm of the fold change) assessed by RNA-seq analysis of: (**A**) wild-type yeast cells overexpressing pRip1 compared to the control (the induction was carried under control of the copper-inducible

bioRxiv preprint doi: https://doi.org/10.1101/2021.05.02.442342; this version posted May 2, 2021. The copyright holder for this preprint (which was not certified by peer review) is the author/funder, who has granted bioRxiv a license to display the preprint in perpetuity. It is made available under aCC-BY-NC-ND 4.0 International license.

promoter (CUP1) for 0, 1, or 8 h), and (**B**) *pam16-3* strain compared to wild-type (cells were grown at a permissive temperature (19 °C) and shifted to restrictive conditions (37 °C) for 1, 4, or 8 h. Differentially expressed genes encoding for the molecular chaperones are indicated in blue. The gene name is displayed for each molecular chaperone if it is detected as differentially expressed (false discovery rate (FDR) 5%, log2 fold change (log2FC) +/-1). (**C**) Table representing all differentially expressed genes in pRip1 samples after 1, 4, and 8 h of overexpression. (**D**) Analysis of expression changes for genes encoding for molecular chaperones using *pam16-3* samples treated as in (B). Up- and down-regulated genes (FDR 5%) are shown in green and pink, respectively. The intensity of the colour shades depends on the level of expression change (log2FC). Genes not detected or those with not statistically significant expression changes are depicted in grey.

Figure supplement 1. Gene changes characterization due to mitochondrial protein import defects.

Source Data 1. Full lists of genes changes in response to pRip1 overexpression.

Source Data 2 Full lists of genes changes in response to pam16-3 overexpression.

Source Data 3 Expression genes matrices in response to pRip1 overexpression.

Source Data 4 Expression genes matrices in response to pam16-3 mutation.

Figure 3. Cytosolic mitochondrial proteins aggregation elicits a molecular chaperone response to restore cellular homeostasis. (**A, D**) Hsp104 and Hsp42 are upregulated in response to mitochondrial protein import impairment. (**A**) Total protein cell extracts from wild-type yeast cells were grown at 24 °C and treated with 0, 5, 10, or 15 µM CCCP for 30 min. (**B**) The quantified changes in the Hsp104 protein expression from (A). Quantified data are

bioRxiv preprint doi: https://doi.org/10.1101/2021.05.02.442342; this version posted May 2, 2021. The copyright holder for this preprint (which was not certified by peer review) is the author/funder, who has granted bioRxiv a license to display the preprint in perpetuity. It is made available under aCC-BY-NC-ND 4.0 International license.

mean ± SEM, for n=3. (**C**) Total protein cell extracts from wild-type (YPH499), *pam16-WT*, *pam16-1*, *pam16-3*, *pam18-WT*, *pam18-1*, *mia40-4WT*, *mia40-4int*, *mia40-3* grown at a permissive temperature (19 °C) and shifted to restrictive conditions (37 °C) for 3 h. (**D**) Total protein cell extracts from wild-type yeast cells and *hsp42-GFP* yeast grown at 24 °C and treated with 0, or 15 µM CCCP for 30 min. (**E-H**) Metastable protein overexpression increases the expression levels of molecular chaperones. Total protein cell extracts expressing indicated metastable proteins or an empty vector control for 4 h showing increased levels of Hsp104 **(E)**, and Hsp42 **(G)**. (**F, H**) Quantitative analysis of Hsp104 (**F**) and Hsp42 (**H**) proteins levels from (E) and (G), respectively. Quantified data are mean ± SEM, for n=3. (**I**) Aggregated metastable proteins co-localise with Hsp42-GFP. Representative confocal microscope images of metastable proteins tagged with the Alexa568 fluorophore in *hsp42-GFP* yeast strain. Scale bar, 2 µm. See Methods for further details. Pearson's correlation coefficient for indicated cells for each condition. (**J**) Total protein cell extracts from wild-type yeast cells and *Δhsp104* yeast grown at 24 °C and treated with 0 or 15 µM CCCP for 30 min. (**K**) SDS-PAGE analysis of the aggregation assay fractions of the samples of wild-type yeast cells and *Δhsp104* yeast grown at 24 °C and treated with 0, or 15 µM CCCP for 30 min. In (A, C-E, G, J, K), samples were separated by SDS-PAGE and identified by western-blotting with specific antisera. p-presequence protein, m-mature protein, *-not specific; (B, F, H) Significance: * p-value<0.05, ** p-value≤0.01; *** p-value≤0.001; **** p≤0.0001, ns- not specific.

Figure supplement 1. Total proteins cell extracts changes due to mitochondrial import defects.

Figure 4. Mitochondrial protein import dysfunction enhances the impairment of cellular homeostasis. (**A-D**) Metastable proteins cause accumulation and aggregation of other mitochondrial precursor proteins. (**A**) Total protein cell extracts from *hsp42-GFP* cells that overnight expressed selected metastable proteins or an empty vector control. The changes for

bioRxiv preprint doi: https://doi.org/10.1101/2021.05.02.442342; this version posted May 2, 2021. The copyright holder for this preprint (which was not certified by peer review) is the author/funder, who has granted bioRxiv a license to display the preprint in perpetuity. It is made available under aCC-BY-NC-ND 4.0 International license.

845 pRip1 (**B**) and pSod2 (**C**) were quantified. Quantified data are mean ± SEM, for n=3. (**D**) SDS-
846 PAGE analysis of the aggregation assays fractions of the *hsp42-GFP* yeast cells overexpressing
847 $Atp2_{FLAG}$ or an empty vector control for 3 h. insoluble - S_{4k} aggregation assay fraction. (**E**)
848 Total protein cell extract from *pam16-3* mutant yeast strains treated with 75 µM of MG132 for
849 1 h in permissive growth conditions and subsequently heat-shocked at 37 °C for 0, 1, 2 or 4 h.
850 (**F-G**) Representative confocal images of the α-Syn WT-GFP (**F**) or A53T-GFP (**G**) aggregates
851 in wild-type (*pam16-WT*) and *pam16-3* yeast strains. α-Syn WT-GFP and A53T-GFP were
852 induced for 4 h at 19 ˚C, and for additional 2 h under 19 ˚C for control, or at 37 ˚C for heat
853 shock. Scale bar, 2 µm. See Methods for further details. Bar plot representation of average
854 number of aggregates per cell. Data are mean ± SEM, n = 57-83 for α-Syn WT-GFP, and n =
855 154-175 for α-Syn A53T-GFP. (**H**) Total cell extracts of the wild-type (*pam16-WT*) and *pam16-*
856 *3* yeast strains expressing α-Syn WT-GFP induced for 4 h at 19 ˚C, and for additional 2 h under
857 19 ˚C for control, or at 37 ˚C for heat shock. (**I**) The quantitative analysis of the pRip1 from
858 (H). Quantified data are mean ± SEM, for n=3. In (A, D, E, H), protein samples were separated
859 by SDS-PAGE and identified by western-blotting with specific antisera. For western-blotting:
860 p-presequence protein, i-intermediate protein, m-mature protein, *-not specific, significance: *
861 p-value<0.05, ** p-value≤0.01; *** p-value≤0.001; ****P≤0.0001, ns- not specific.
862 **Figure supplement 1.** Effects of mitochondrial protein import dysfunction on cellular
863 homeostasis.
864
865
866 **Figure 5. Mitochondrial dysfunction results in accumulation of Aβ aggregates in *C.***
867 ***elegans*.** (**A-C**) Mitochondrial dysfunction stimulates aggregation of model proteins in *C.*
868 *elegans*. (**A**) Confocal images of worms expressing wrmScarlet and GFP in body wall muscle
869 [pmyo-3::wrmScarlet+pmyo::GFP]. Zoomed image presented in the white squere. Scale bar,

bioRxiv preprint doi: https://doi.org/10.1101/2021.05.02.442342; this version posted May 2, 2021. The copyright holder for this preprint (which was not certified by peer review) is the author/funder, who has granted bioRxiv a license to display the preprint in perpetuity. It is made available under aCC-BY-NC-ND 4.0 International license.

20 µm. (**B**) Number of RFP aggregates present at different days of adulthood of strain [pmyo-3::wrmScarlet + pmyo-3::GFP] upon *dnj-21* RNAi. Tested worms, emty vector = 14-16, *dnj-21* RNAi = 8-16. (**C**) Number of GFP aggregates present at different days of adulthood of strain [pmyo-3::wrmScarlet + pmyo-3::GFP] upon *dnj-21* RNAi. Tested worms, emty vector = 14-16, *dnj-21* RNAi = 8-16. (**D**) Motility of model PD strain (expressing α-synuclein::YFP in the body wall muscle) or control strain (YFP, expressing YFP in the body wall muscle) upon silencing of *dnj-21*; emty vector was used as control. Data were obtained using an automated body bend assay. Data are mean ± SEM with at least n=700 for each condition. (**E**) Aggregation in native conditions in worms expressing Aβ upon *dnj-21* RNAi. Worms were cultured in 20 ˚C or with shift temperature to 22 ˚C or 25 ˚C. (**F**) Aβ levels calculated from native aggregation (E). Data are mean ± SD, n=3. (**G**) Motility in worms expressing Aβ and GFP upon *dnj-21* RNAi. Data are mean ± SEM, n=50 worms per each condition, overall differences between conditions were assessed by unpaired t-test assuming equal variances. Significance: * p-value<0.05, ** p-value≤0.01; *** p-value≤0.001; **** p≤0.0001, ns-not significant.

Figure supplement 1. Scheme and controls for experiments on mitochondrial dysfunction in *C. elegans* that results in Aβ accumulation.

bioRxiv preprint doi: https://doi.org/10.1101/2021.05.02.442342; this version posted May 2, 2021. The copyright holder for this preprint (which was not certified by peer review) is the author/funder, who has granted bioRxiv a license to display the preprint in perpetuity. It is made available under aCC-BY-NC-ND 4.0 International license.

Figure Supplement Legends

Figure 1–figure supplement 1. Aggregation propensity characterisation of mitochondrial proteins. The protein sequences and information about mitochondria targeting presequences were acquired from Saccharomyces Genome Database and verified using Mitofates (Fukasawa et al., 2015) and MitoProt (Claros & Vincens, 1996) software. Protein solubility was analysed using CamSol (Sormanni, Aprile, & Vendruscolo, 2015) software. Proteins and sequence residues with score value of < -1 are poorly soluble and indicated as a potential self-assembly hotspots (red). Value > 1 characterizes highly soluble proteins and sequence residues (blue).. TMDs, Transmembrane domains; IMS, Inter membrane space; IM, inner membrane.

Figure 1–figure supplement 2. Supersaturated nuclear-encoded mitochondrial proteins aggregate in the cytosol and stimulate growth defects. (**A**) Schematic representation of the aggregation assay. (**B, C**) Metastable proteins aggregate in the cell. SDS-PAGE analysis of the aggregation assays fractions of the wild-type yeast cells overexpressing $Atp2_{FLAG}$, $Atp20_{FLAG}$ (**B**) and $Cox8_{FLAG}$, $Qcr8_{FLAG}$, $pRip1_{FLAG}$, $iRip1_{FLAG}$, $mRip1_{FLAG}$, $Cor1_{FLAG}$, $Mas1_{FLAG}$, $Cox12_{FLAG}$ and $Qcr6_{FLAG}$ (**C**) for 3 h at 28 °C. (**D**) Metastable proteins exhibit a temperature-sensitive phenotype. Each protein expressing strain was subjected to consecutive tenfold dilutions, spotted on selective medium agar plates with glucose as the main carbon source at 28 °C and 37 °C. (**E**) Cartoon representation of the Rip1, Sod2, and Mdh1 mitochondrial proteins containing their presequences. (**F**) Total protein cell extract from wild-type (*WT*) and *pam16-3* mutant yeast strains grown at permissive temperature (19 °C), and shifted to restrictive conditions of 37 °C for 0, 1, 3 or 5 h.

p-presequence protein, m-mature protein, i- intermediate, *-not specific, aa-amino acid.

bioRxiv preprint doi: https://doi.org/10.1101/2021.05.02.442342; this version posted May 2, 2021. The copyright holder for this preprint (which was not certified by peer review) is the author/funder, who has granted bioRxiv a license to display the preprint in perpetuity. It is made available under aCC-BY-NC-ND 4.0 International license.

Figure 2–figure supplement 1. Gene changes characterization due to mitochondrial protein import defects. (**A**) Bar plots representing the total number of detected gene transcripts in *pam16-3* and pRip1 samples by RNA sequencing. The proportions of significant genes (FDR 5%) are shown in grey shades (Statistically significant), while the proportions of differentially expressed features in the *pam16-3* and pRip1 samples (FDR 5%; log2FC +/- 1) are shown in green (up-regulated) and pink (down-regulated). The number of genes and in each group is indicated. (**B-C**) Kyoto Encyclopedia of Genes and Genomes (KEGG) enrichment analysis for differentially expressed genes for pRip1 (**B**) and *pam 16-3* (**C**) samples, respectively. The results are shown as a negative log10 P-value after Bonferroni correction. Bars in green indicate KEGG terms enriched for up-regulated genes, while the pink bars represent the KEGG terms for the down-regulated features. No KEGG terms were identified for down-and up-regulated pRip1 and *pam16-3* genes, respectively. (**D**) Bar plots representing the proportion of mitochondrial genes encoding the high confidence mitochondrial proteome (HCMP) in each set. The proportions of significant genes (FDR 5%) are shown in grey shades (Statistically significant), while the proportions of differentially expressed features in the *pam16-3* and pRip1 samples (FDR 5%; log2FC +/- 1) are shown in green (up-regulated) and pink (down-regulated). The number of genes and in each group is indicated. The number of genes in each fraction is indicated in parenthesis. (**E**) Expression analysis of the selected chaperone genes based on the RNAseq analysis in *pam16-3* strains. Cells were grown at permissive temperature 19 °C and were shifted to restrictive conditions of 37 °C for 1, 4 and 8 h. Dark shades indicate the expression level in *pam16-3* compared to wild-type strains, whereas the light shades show the expression changes in wild-type samples triggered by the heat shock response. To estimate the transcriptional changes induced by the elevated temperature, the wild-type samples incubated for 37 °C for 1, 4, and 8 h were compared against no treated wild-type samples (0h). Arrows

bioRxiv preprint doi: https://doi.org/10.1101/2021.05.02.442342; this version posted May 2, 2021. The copyright holder for this preprint (which was not certified by peer review) is the author/funder, who has granted bioRxiv a license to display the preprint in perpetuity. It is made available under aCC-BY-NC-ND 4.0 International license.

indicate chaperones for which the biggest increase in chaperones' genes levels were observed due to mitochondrial import defect, when compared to changes just due to the heat shock. (**F**) Analysis of expression changes for genes related to the MitoCPR[13] response based on the RNAseq analysis in *pam16-3* strains. Up- and down-regulated genes (FDR 5%) are shown in green and pink, respectively. The intensity of the colour shades depends on the level of expression change (log2Fold Change).

Figure 3–figure supplement 1. Total proteins cell extracts changes due to mitochondrial import defects. (**A**) Total protein cell extracts from wild-type yeast cells yeast grown at 24 °C and treated with 0, 5, 10, or 15 µM CCCP for 15 min. (**B**) Total protein cell extracts from wild-type (YPH499), *pam16-WT*, *pam16-1*, *pam16-3*, *pam18-WT*, *pam18-1*, *mia40-4WT*, *mia40-4int*, *mia40-3* grown at 19 °C and shifted to of 37 °C for 6 h.

Figure 4–figure supplement 1. Effects of mitochondrial protein import dysfunction on cellular homeostasis. (**A**) The presence of metastable proteins results in the cytosolic accumulation of other mitochondrial precursors proteins. The SDS-PAGE analysis of the total protein cell extracts from *hsp42-GFP* yeast cells that expressed $Atp2_{FLAG}$, $Cox8_{FLAG}$ or an empty vector control for 3 h, corresponding to aggregation assay from **Figure 4D** and **Figure 4–figure supplement 1B.** (**B**) SDS-PAGE analysis of the aggregation assays fractions of the *hsp42-GFP* yeast cells overexpressing $Cox8_{FLAG}$ or an empty vector control for 3 h. insoluble - S_{4k} aggregation assay fraction. (**C**) SDS-PAGE analysis of the aggregation assay fractions of the *pam16-3* mutant yeast strain grew at permissive temperature 19 °C to the mid-logarithmic phase. Cells were treated with 75 µM MG132 for 1 h and heat-shocked at 37 °C for 0, 3 or 5 h. (**D, E**) The wild-type (*pam16-WT*) and *pam16-3* yeast strains expressing α-Syn WT-GFP (**D**)

bioRxiv preprint doi: https://doi.org/10.1101/2021.05.02.442342; this version posted May 2, 2021. The copyright holder for this preprint (which was not certified by peer review) is the author/funder, who has granted bioRxiv a license to display the preprint in perpetuity. It is made available under aCC-BY-NC-ND 4.0 International license.

or A53T-GFP (**E**) samples used for the confocal images presented in **Figure 4F** and **4G**. were subjected to the SDS-PAGE analysis of the total protein cell extracts.

bioRxiv preprint doi: https://doi.org/10.1101/2021.05.02.442342; this version posted May 2, 2021. The copyright holder for this preprint (which was not certified by peer review) is the author/funder, who has granted bioRxiv a license to display the preprint in perpetuity. It is made available under aCC-BY-NC-ND 4.0 International license.

Figure 5–figure supplement 1. Scheme and controls for experiments on mitochondrial dysfunction in C. elegans that results in Aβ accumulation. (**A**) RNAi silencing effectiveness, protein levels upon *dnj-21* RNAi in worms strain [pmyo-3::wrmScarlet + pmyo::GFP]. (**B**) Scheme of temperature shifts performed during worm culture in the experiments presented in **Figure 5E-G,** and **Figure 5–figure supplement 1D-F**. (**C**) Protein levels in worms expressing Aβ peptieds upon *dnj-21* RNAi. Worms were cultured with indicated temperature shift. (**D**) SDS-PAGE analysis of the aggregate levels in worms expressing Aβ peptieds upon *dnj-21* RNAi (n=3 biological replicates). Worms were cultured in 20 ˚C or with temperature shift to 22 ˚C or 25 ˚C. (**E**) Aβ levels calculated from SDS-PAGE analysis of the aggregate in (D). Data are mean ± SD, n=3, overall differences between conditions were assessed by unpaired t-test assuming unequal variances. (**F**) Motility in worms expressing GFP upon *dnj-21* RNAi. Data are mean ± SEM, overall differences between conditions were assessed by unpaired t-test assuming equal variances, for culture in 20 ˚C n=35 worms; for culture with 22 ˚C shift n=60 worms, for culture with 25 ˚C n=50 worms. Significance: * p-value<0.05, ** p-value≤0.01; *** p-value≤0.001; **** p≤0.0001, ns-not significant.

Supplementary file 1. Nucleotides used to clone protein coding sequences and CUP1 promoter into pESC-URA.

Supplementary file 2. List of plasmid used in this study.

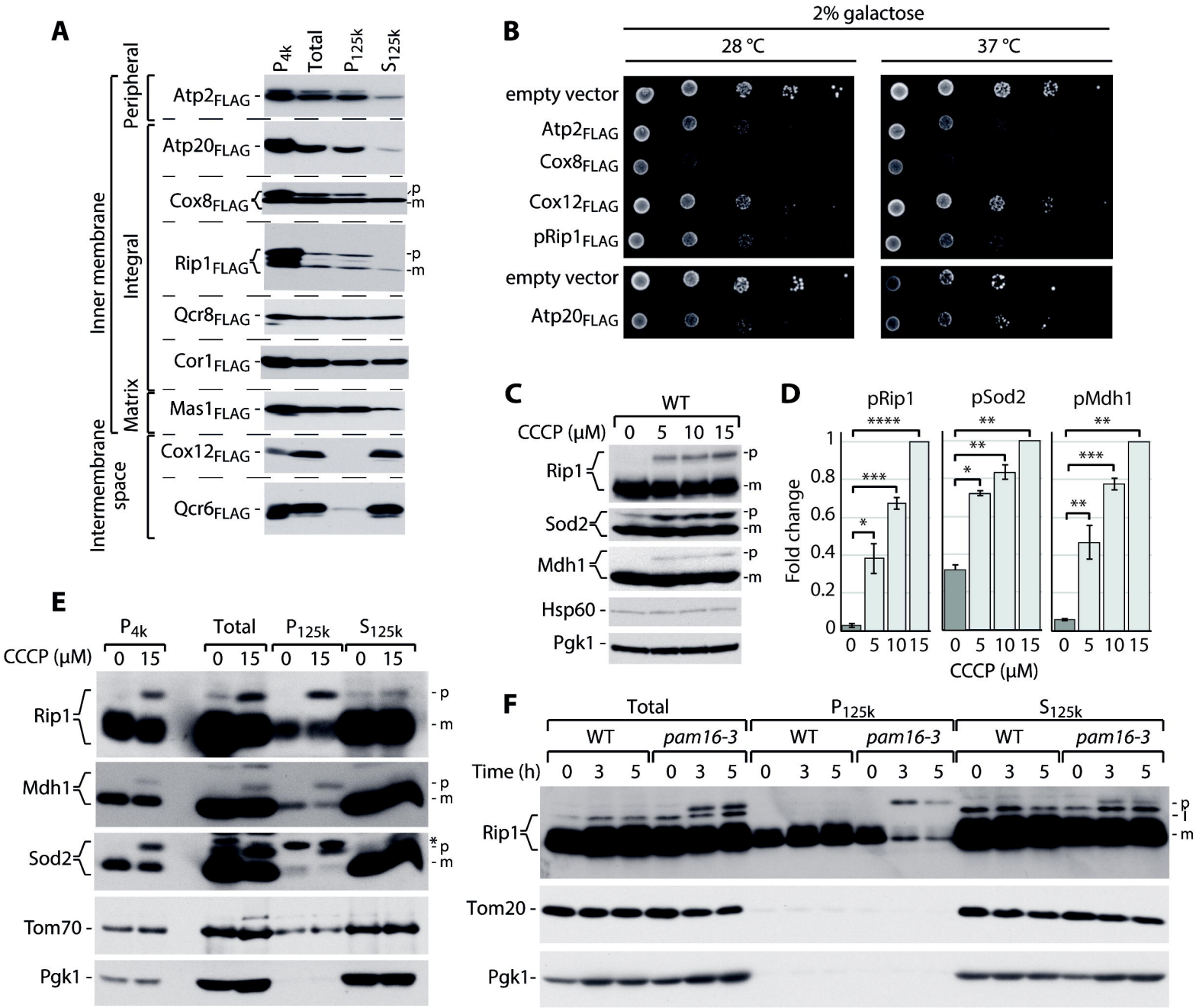

Figure 1. Nowicka et al.

Human homologs	Protein name (ORF name)	Localization	Amount of TMDs	Intrinsic residue solubility along amino acid sequence	Intrinsic solubility score	Mitochondria targeting sequence
ATP5B	Atp2 (YJR121W)	peripheral IM	0	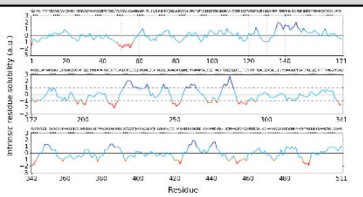	0.4783	N-terminal cleavable presequence
ATP5L	Atp20 (YPR020W)	IM	1	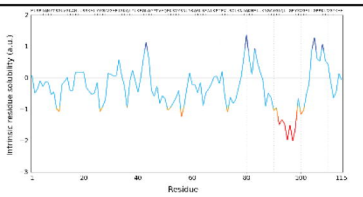	0.9556	N-terminal non-cleavable sequence
COX7C	Cox8 (YLR395C)	IM	1	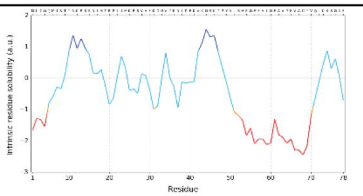	-0.2763	N-terminal cleavable presequence
COX6B1	Cox12 (YLR038C)	IMS	0	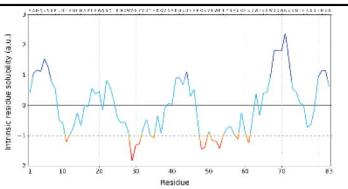	1.2939	Cystein motifs
UQCRFS1	Rip1 (YEL024W)	IM	2	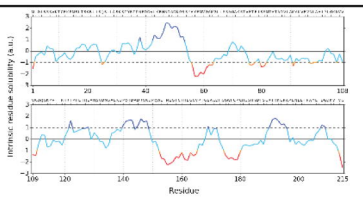	0.4783	N-terminal cleavable presequence
UQCRH	Qcr6 (YFR033C)	IMS	0	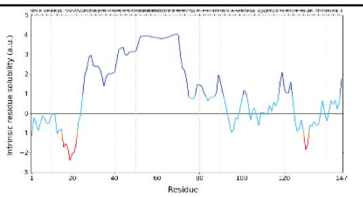	4.1091	Unknown
UQCRQ	Qcr8 (YJL166W)	IM	1	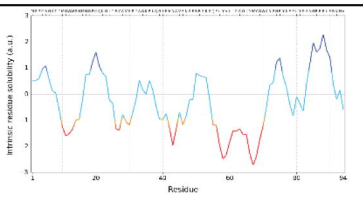	0.0079	N-terminal non-cleavable sequence
UQCRC1	Cor1 (YBL045C)	IM	0	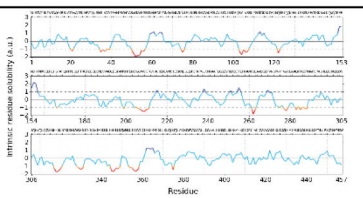	0.3800	N-terminal cleavable presequence

Figure 1 - figure supplement 1. Nowicka et.al.

bioRxiv preprint doi: https://doi.org/10.1101/2021.05.02.442342; this version posted May 2, 2021. The copyright holder for this preprint (which was not certified by peer review) is the author/funder, who has granted bioRxiv a license to display the preprint in perpetuity. It is made available under aCC-BY-NC-ND 4.0 International license.

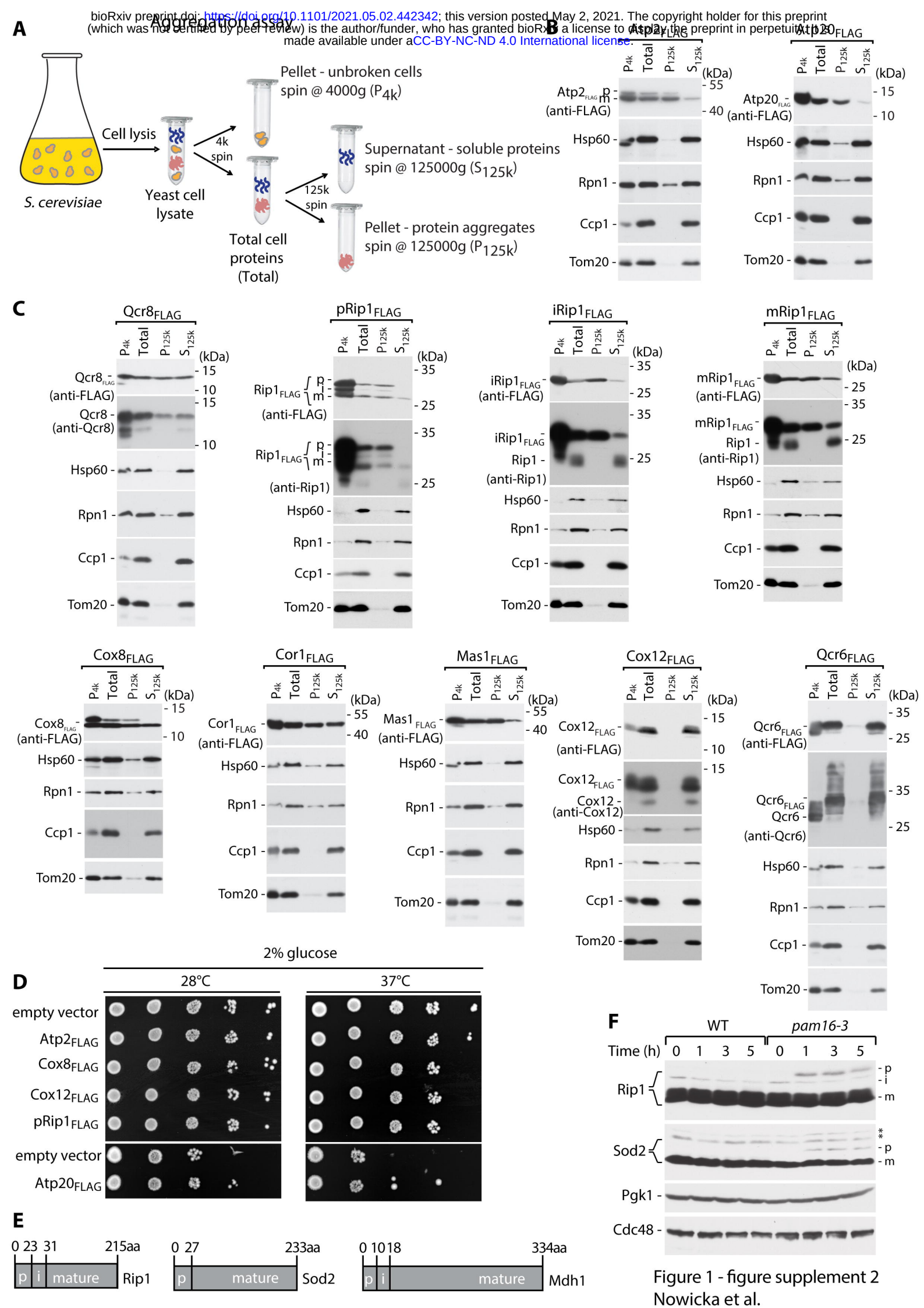

Figure 1 - figure supplement 2
Nowicka et al.

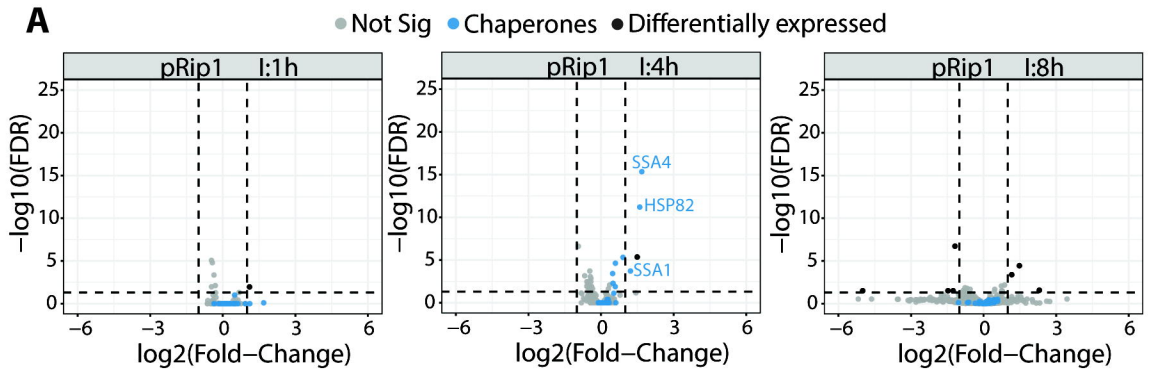

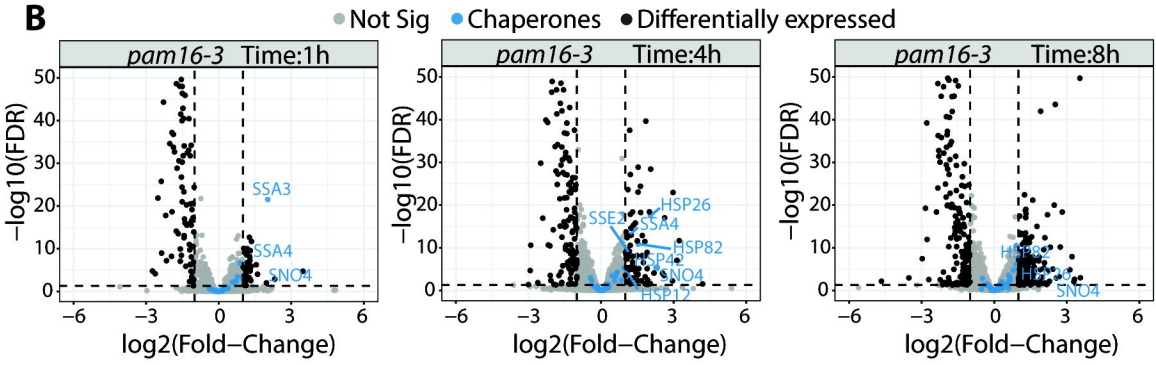

C

Gene	log2FC
1h	
RIP1	8.6
RUF5.2	1.1
4h	
RIP1	7
BTN2	2
SSA4	1.7
HSP82	1.6
PDR5	1.5
SSA1	1.2
8h	
RIP1	6.9
RSB1	2.3
PDR5	1.5
YLR413W	1.2
POT1	-1.2
DLD3	-1.3
AGP3	-1.5
PDC6	-5

Rip1 genes with significant change

log2FC

-10 -5 0 5 10

D

Time (h)	1	4	8
Gene	log2FC		
SNO4	2.3	3.1	2.7
HSP26	0.9	2	1.3
HSP82	1	1.5	1.2
HSP42	1	1.2	
SSA4	1.3	1.1	0.9
SSE2	0.9	1.1	
HSP12	0.7	1.1	
HSP32	0.9	0.9	
HSP104	0.7	0.8	
HSP33	0.7	0.8	
AHA1	0.6	0.6	0.7
SIS1	0.6	0.6	
STI1	0.6	0.6	
CCS1		0.5	
ECM10		0.5	0.3
HSP10	0.7	0.5	
YDJ1		0.5	0.9
SGT2	0.5	0.4	
HSP60	0.7	0.4	
MDJ1	0.6	0.4	
SSE1		0.3	0.6
CDC37		-0.4	-0.3
SCJ1		-0.7	
JEM1		-0.7	0.3
LHS1		-0.8	

pam16-3: Chaperones genes with significant change

log2FC

-4 -2 0 2 4

Figure 2. Nowicka et al.

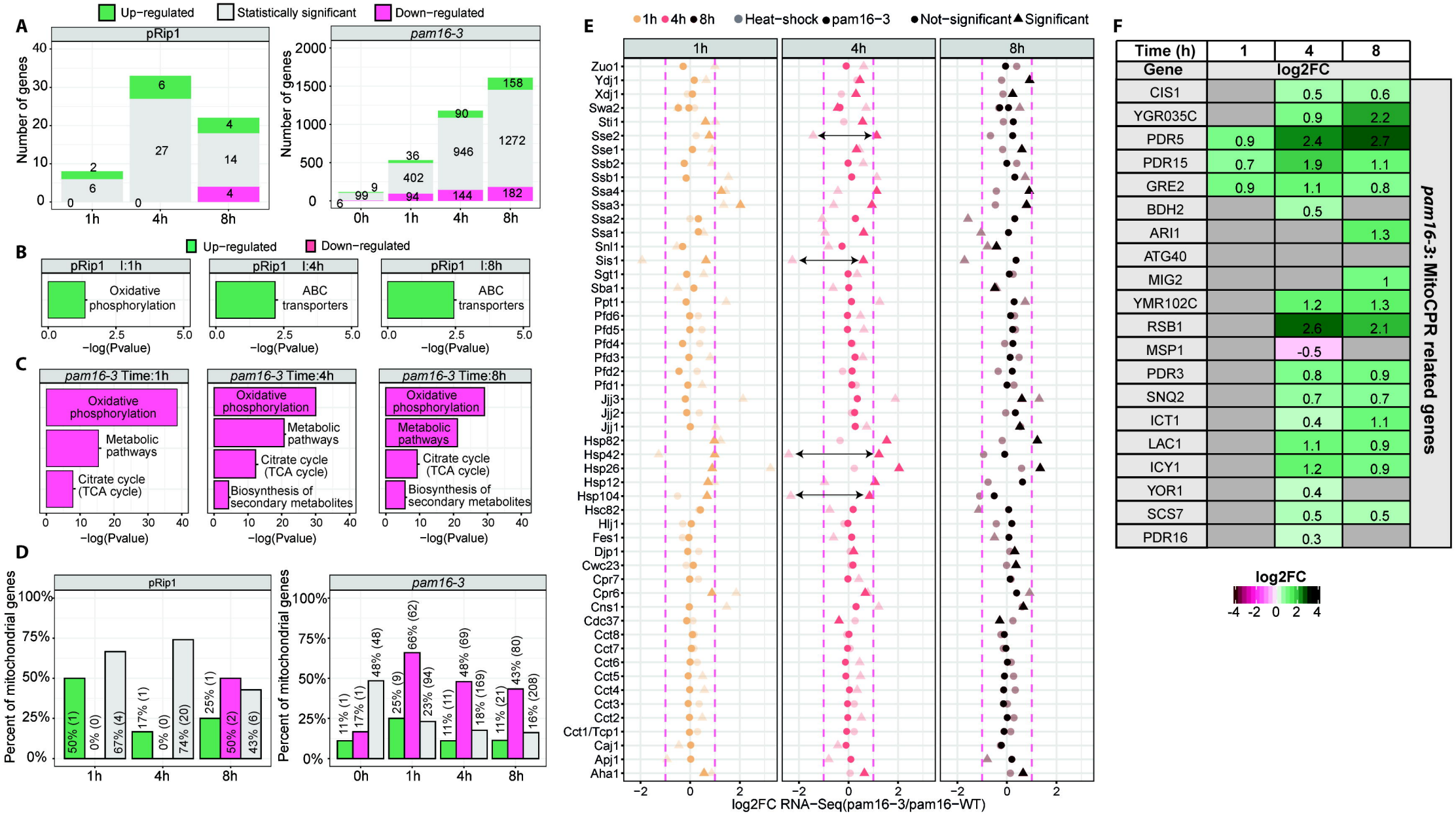

Figure 2 - figure supplement 1. Nowicka et al.

bioRxiv preprint doi: https://doi.org/10.1101/2021.05.02.442342; this version posted May 2, 2021. The copyright holder for this preprint (which was not certified by peer review) is the author/funder, who has granted bioRxiv a license to display the preprint in perpetuity. It is made available under aCC-BY-NC-ND 4.0 International license.

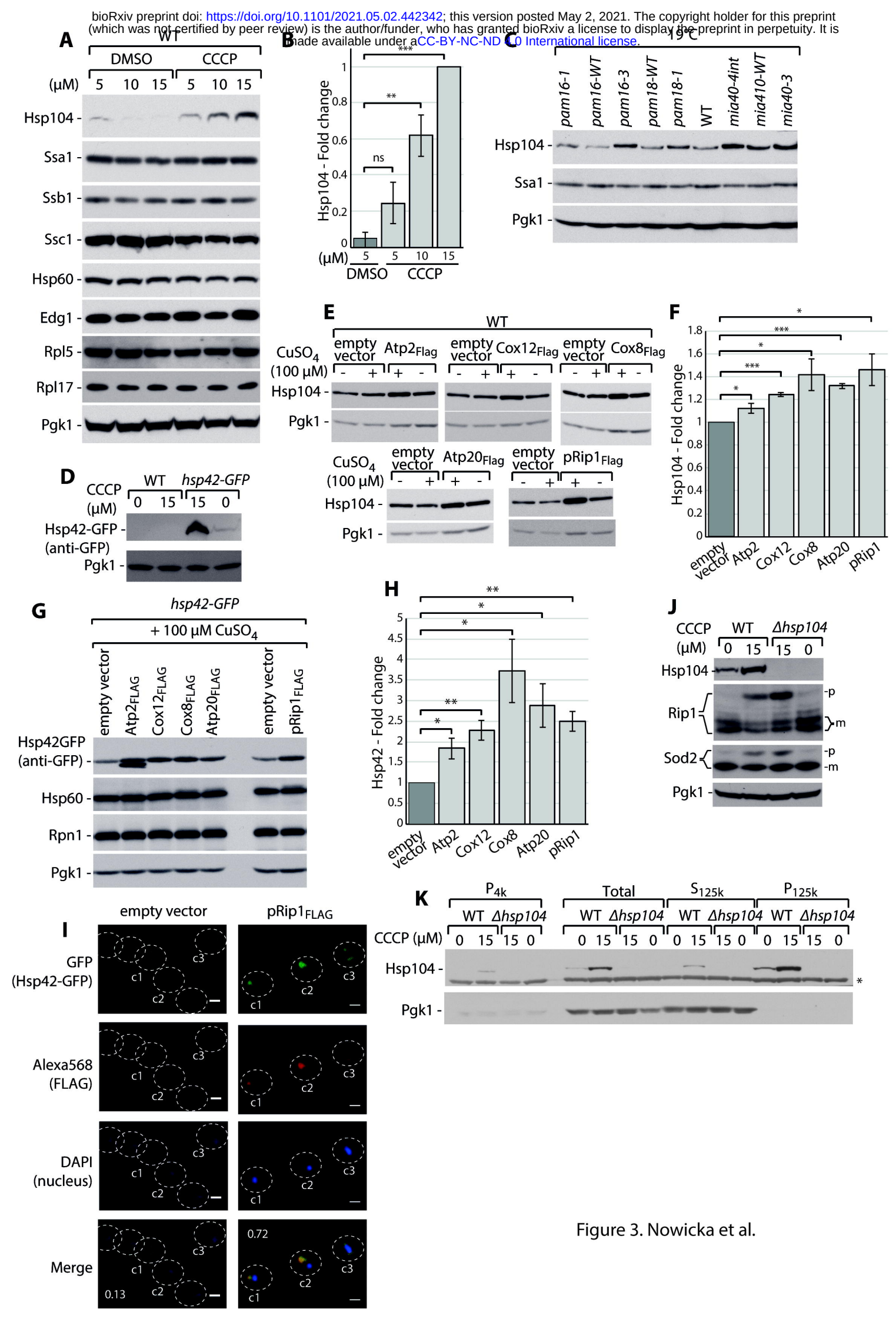

Figure 3. Nowicka et al.

bioRxiv preprint doi: https://doi.org/10.1101/2021.05.02.442342; this version posted May 2, 2021. The copyright holder for this preprint (which was not certified by peer review) is the author/funder, who has granted bioRxiv a license to display the preprint in perpetuity. It is made available under aCC-BY-NC-ND 4.0 International license.

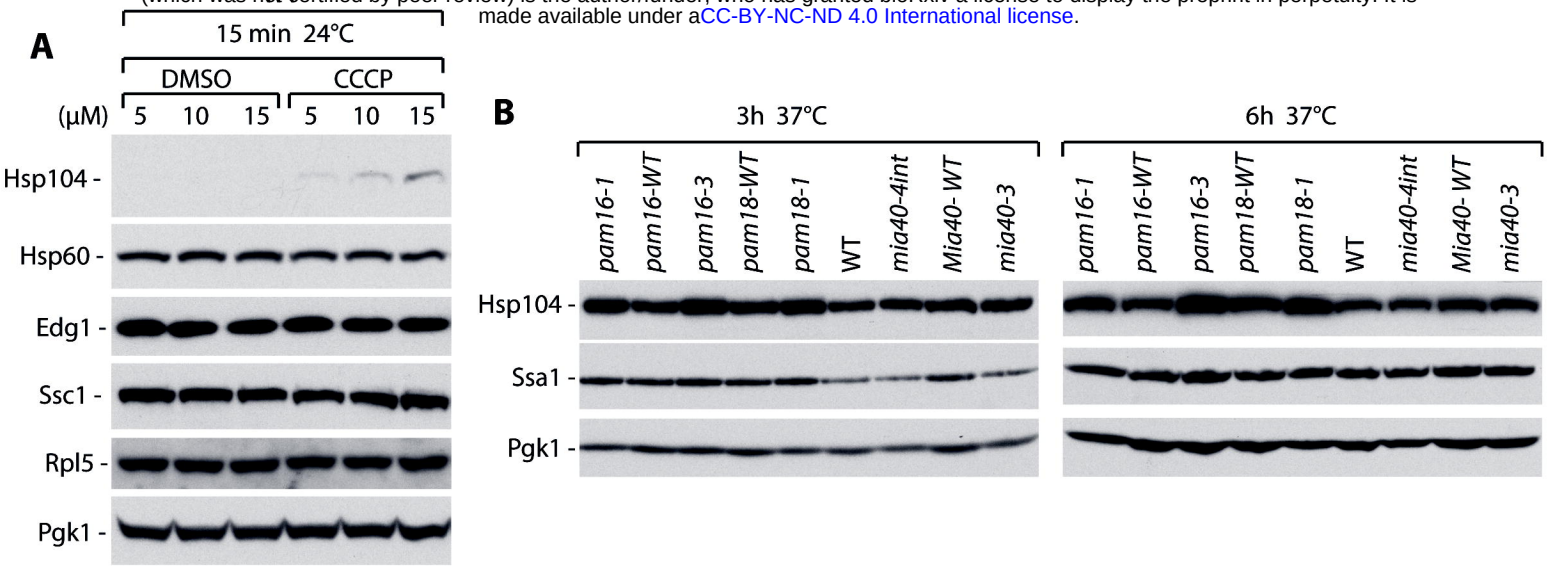

Figure 3 - figure supplement 1. Nowicka et al.

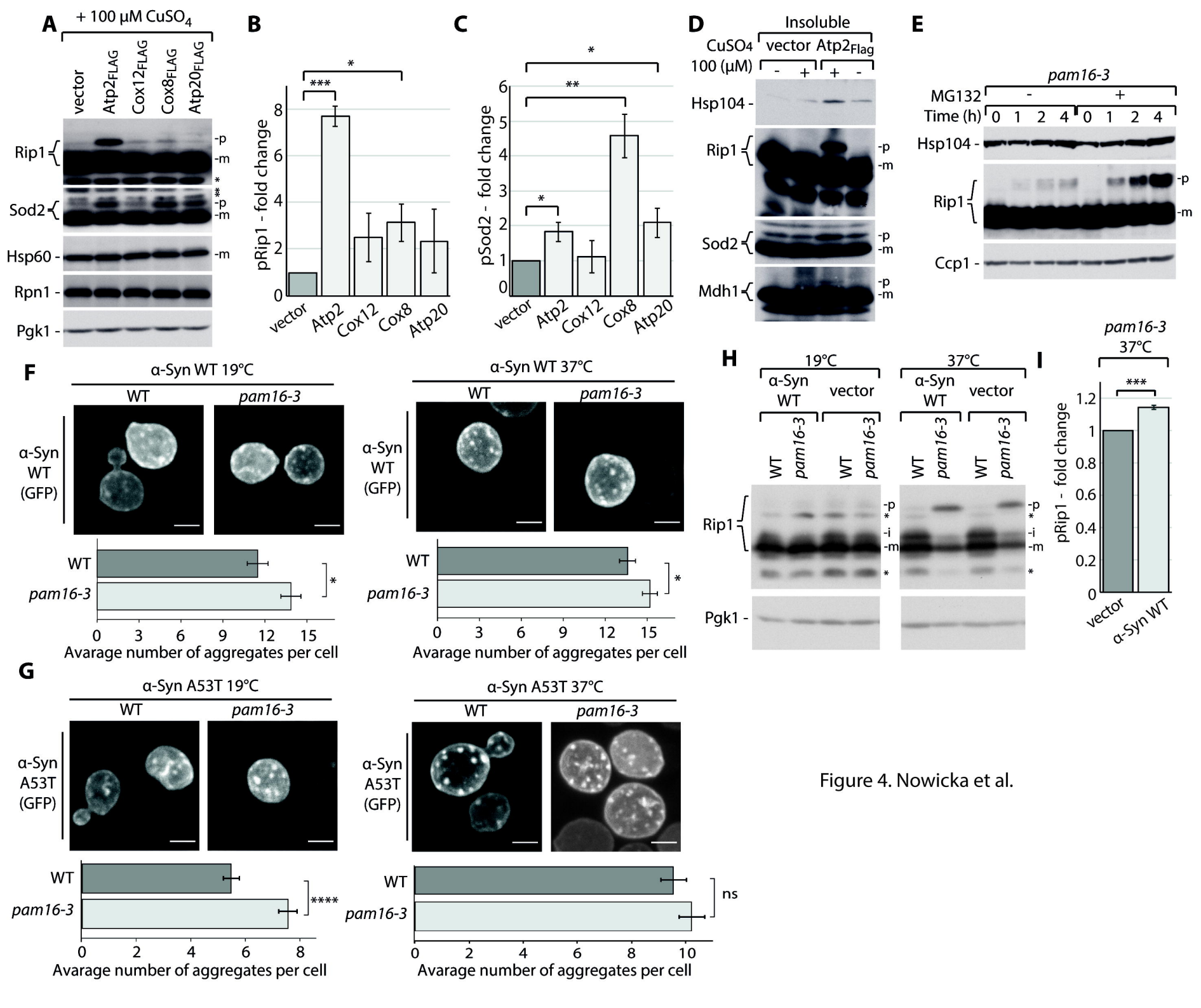

Figure 4. Nowicka et al.

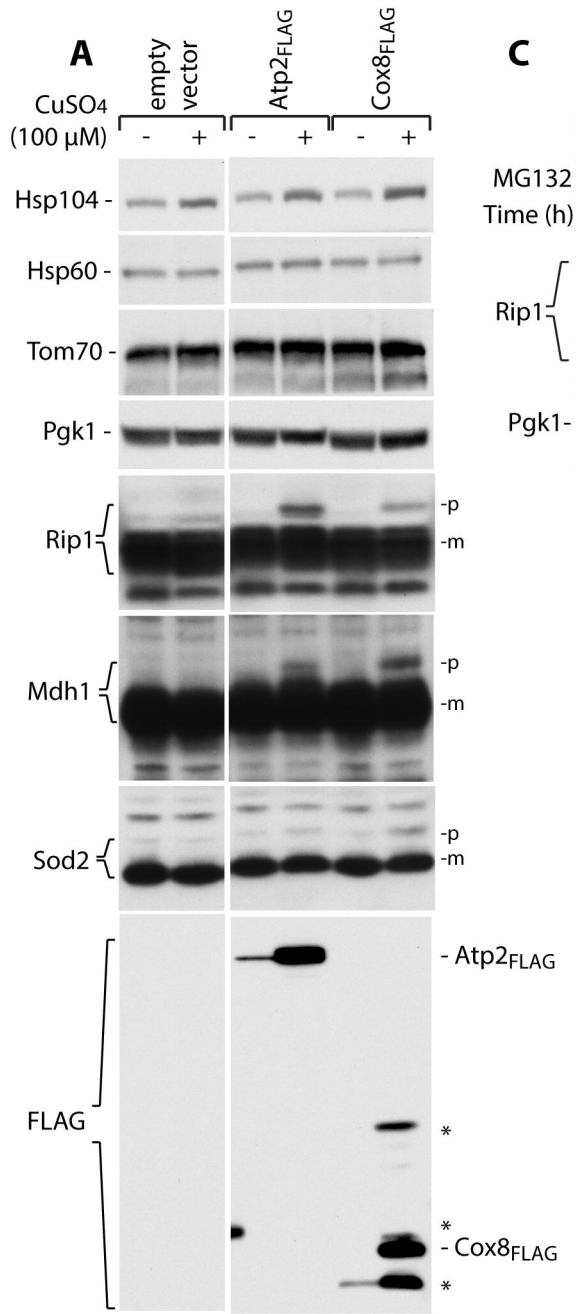

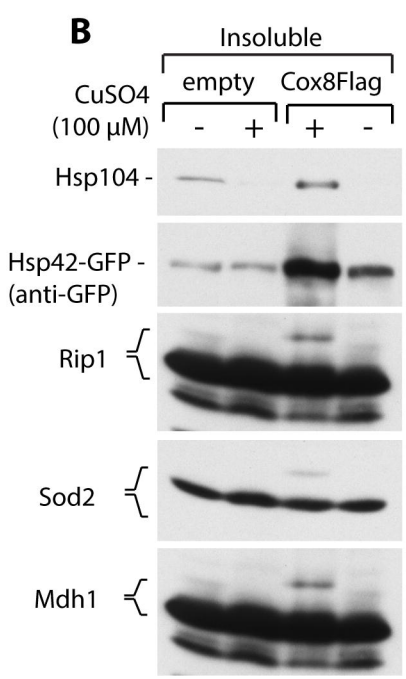

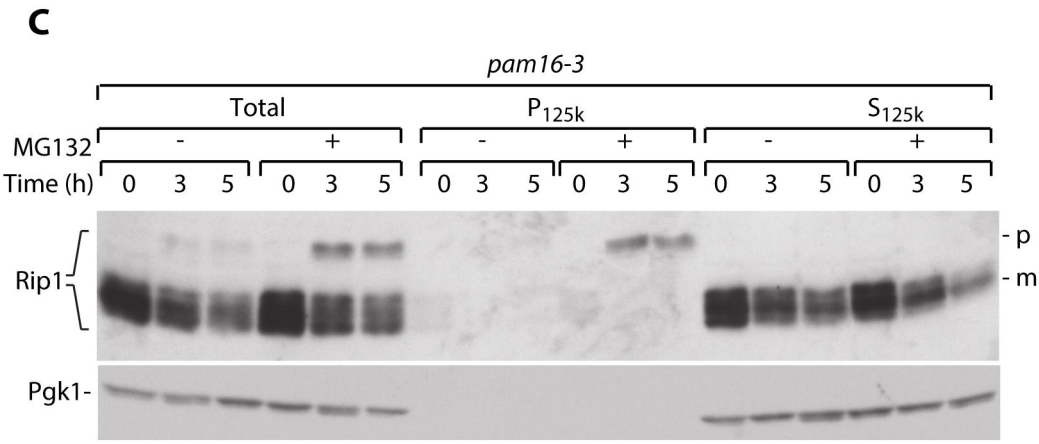

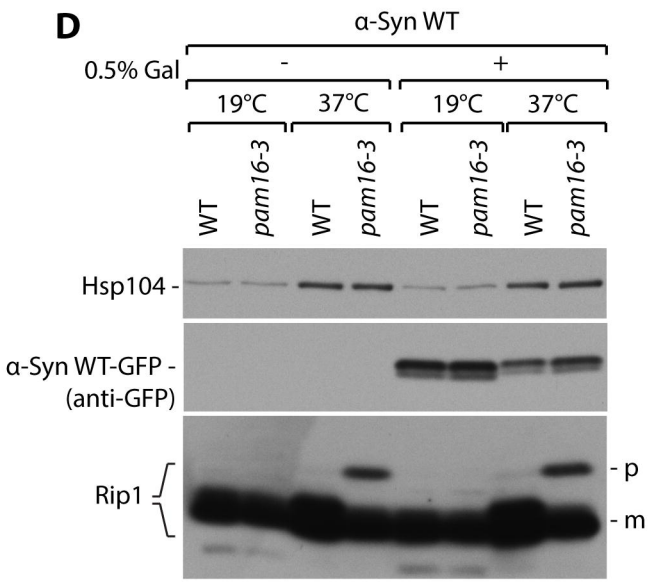

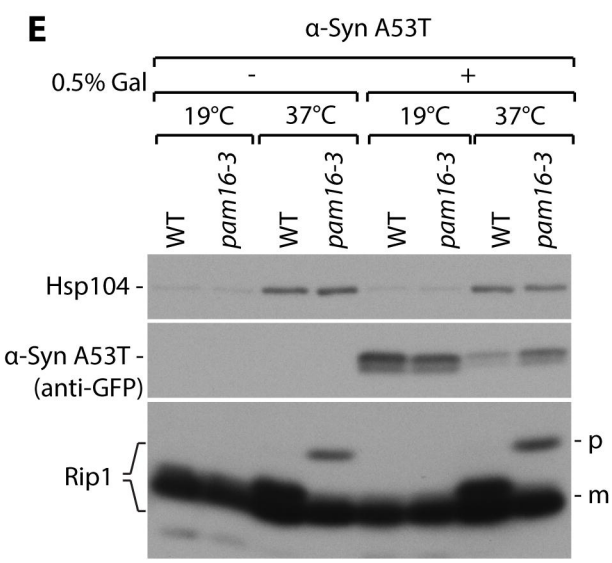

Figure 4 - figure supplement 1. Nowicka et al.

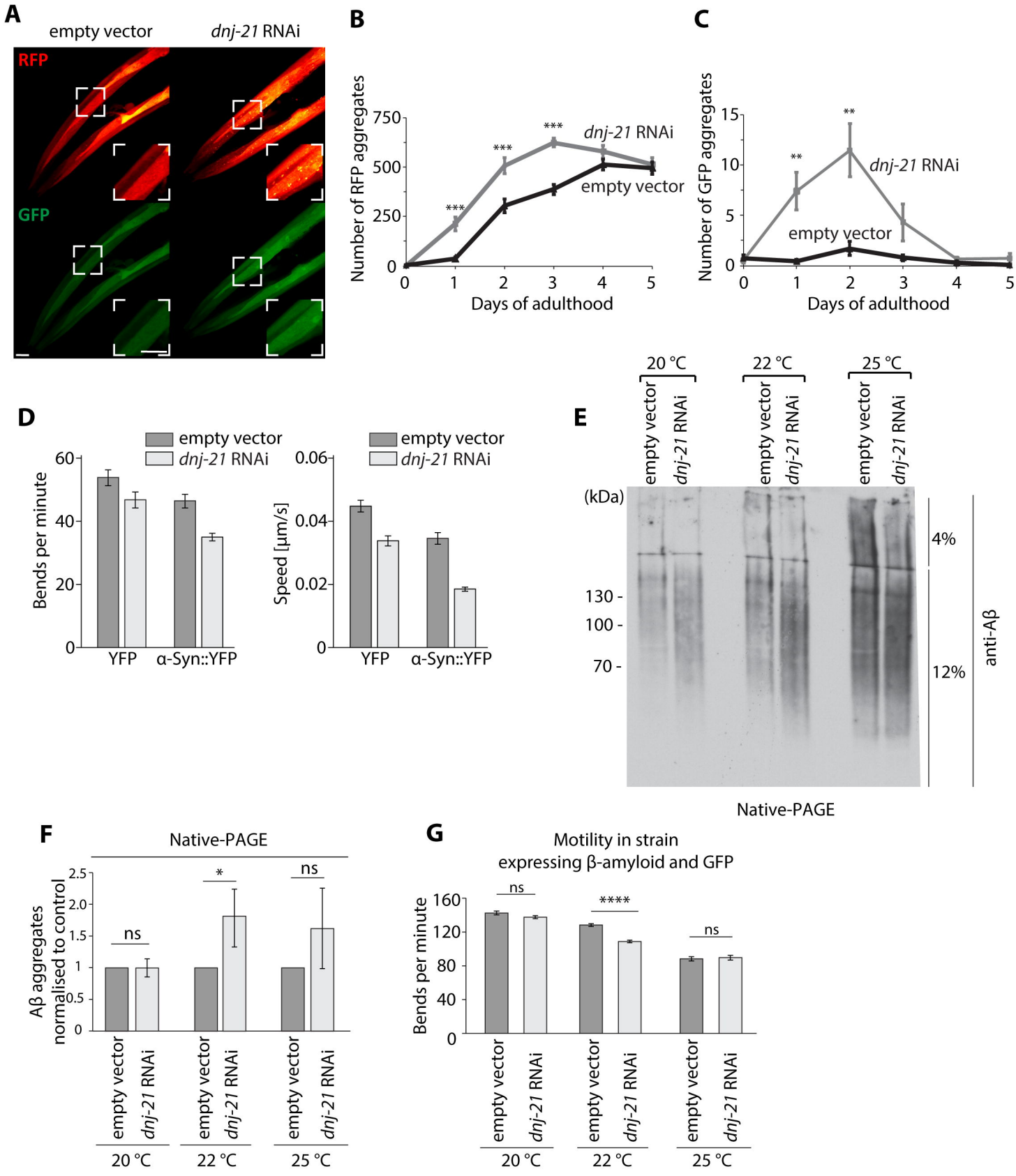

Figure 5. Nowicka et al.

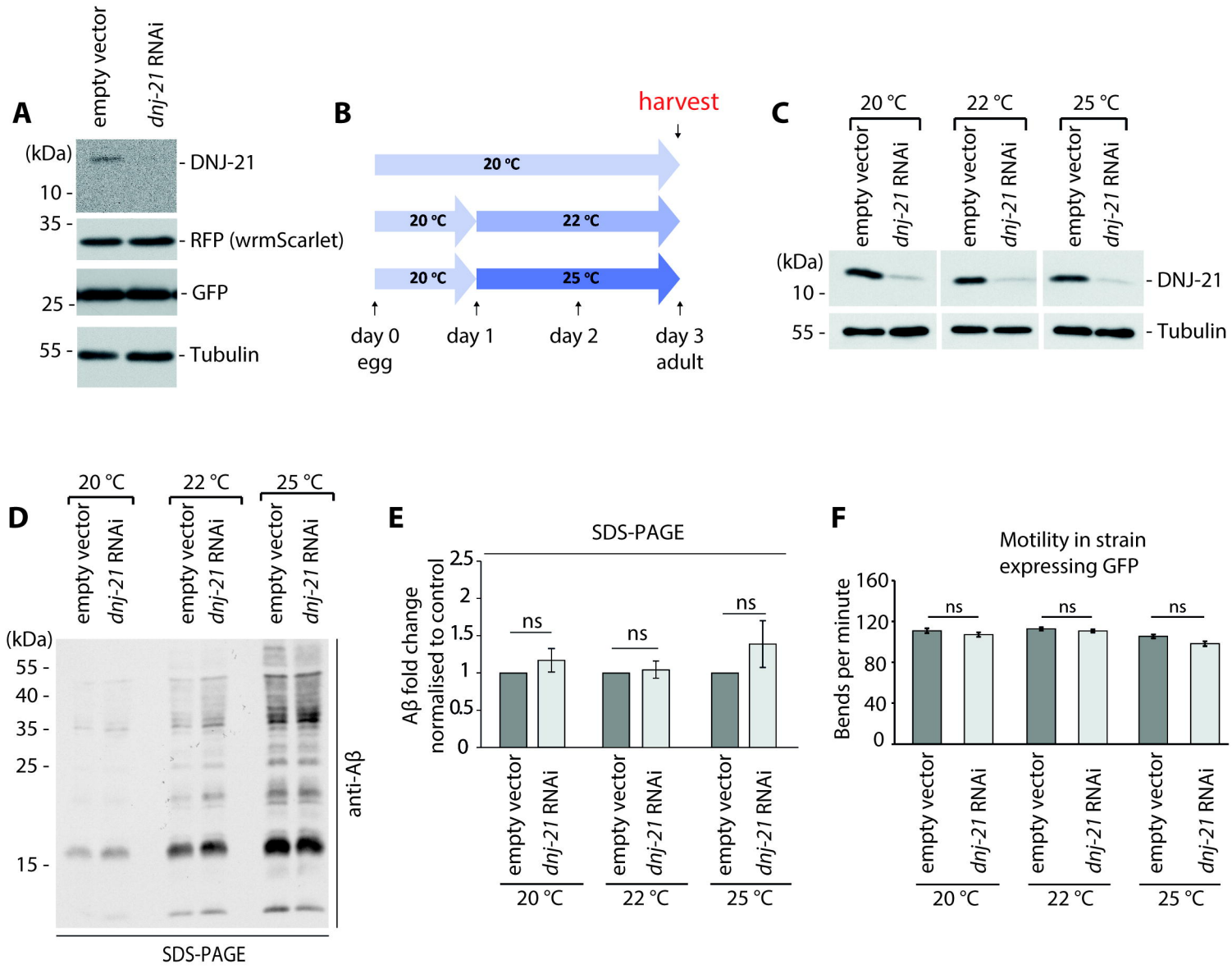

Figure 5 - figure supplement 1. Nowicka et al.